Measurement of the temperature dependence of the Buckingham effect (electric-field-gradient-induced birefringence) in gases.

by
Naven Chetty
BSc(Hons)(Physics)

Submitted in partial fulfilment of the requirements
for the degree of PhD in the
School of Physics,
University of KwaZulu-Natal
Pietermaritzburg

9 March, 2009

Contents

List of Figures

List of Tables

Declaration

This thesis describes the work undertaken at the University of KwaZulu-Natal, Pietermaritzburg, under the supervision of Dr V. W. Couling between January 2004 and August 2008.

I declare that this work is the result of my own research, unless specifically indicated to the contrary in the text. This thesis has not been submitted in any form for any degree or examination to any other university.

Signed: _____ Date: _____

I hereby certify that this statement is correct

Signed: _____ Date: _____

Dr V. W. Couling (Supervisor)

Dedication

It is with great sadness that I dedicate this thesis to my late granny **Mrs Logie Moodley**. This incredible woman was born on the 9 October 1933 and passed away on the 2 February 2009. Her inspirational role in my life cannot be described with mere words and this dedication is a way of ensuring that her legacy and influence in my life is never forgotten. I am deeply saddened that she is not here to share in my joy at the completion of this work. Rest in Peace Ma, until we meet again.

Abstract

The aim of this research project was to assemble an apparatus to measure the electric quadrupole moments of gas molecules using the technique of electric-field-gradient-induced birefringence, or the Buckingham effect. Comprehensive research by various workers in the field has shown that this technique provides the only direct means of obtaining the quadrupole moment of a molecule.

Theory has shown that the most accurate determination of the electric quadrupole moment is through a study of the temperature dependence of the effect. This not only allows for the quadrupole moment to be obtained but also enables the temperature-independent quadrupole hyperpolarisability term to be extracted. Both the quadrupole moment and the hyperpolarisabilty provide valuable information in a variety of applications, including intermolecular forces, electrostatic potentials and non-linear optical phenomena.

This thesis fully describes the apparatus used in these measurements, in-

cluding a description of the custom built oven that allowed for measurements to be performed over a temperature range spanning from 25°C up to 200°C. Results for the quadrupole moments and quadrupole hyperpolarisabilities of carbon dioxide, carbon monoxide, nitrous oxide and hydrogen are presented, together with a quadrupole moment for carbonyl sulphide from room-temperature measurements. Wherever possible, the results of this work are compared to previously published experimental and theoretical data.

Acknowledgments

An experimental research project is the most challenging any researcher can embark on, and it requires the input, support, assistance, advice, and experience of many people to ensure its success. With this in mind I wish to express a sincere vote of appreciation to all those whose assisted me in the past four years on this project. In particular I must acknowledge :

- My supervisor, Dr V. W. Couling for his guidance and helpful discussion throughout this project. His knowledge and inspiration proved invaluable and his kindness and understanding in my time of need is deeply appreciated and no amount of words can express my sincere gratitude.

- Prof. R. E. Raab for his time and dedication in reading this thesis. His help in many aspects of this project and funding the purchase of the carbon monoxide gas used in this work is greatly appreciated. The many helpful discussions throughout this work, especially when things would not work, will not easily be forgotten.

- Prof. C. Graham is sincerely thanked for his insightful advice into many aspects of this project.

- Messers A. Cullis, G. Dewar, J. Woodley, and J. Wilkinson of the Electronics Centre (EC) are thanked for building and maintaining most of electronics used in this project. The time and boundless dedication they provided to ensure that the equipment performed at its peak are most appreciated. This project benefited greatly from their expertise and I am deeply grateful for all the help and assistance they have provided over the years.

- Messers C. Morewood, D. Liebrandt, R. Hendriks, T. Hodge, D. Wiener, and Lawrence of the Mechanical Instrument Workshop (MIW) are thanked for their immense contribution to the mechanical and structural side of the project. Their assistance with building, repairing, and modifying the apparatus is noted and appreciated, and so too are their helpful design suggestions on many aspects of the project.

- Mr R. Sivraman, Technician in the School of Physics, deserves a special mention for his considerable help throughout this project. His selflessness in assisting me with any aspect of the project, regardless of how dirty or time consuming it was, is deeply appreciated.

- Mr K. Penzhorn, Senior Technician in the School of Physics, is also acknowledged. His great contribution in manufacturing, modifying and

repairing parts of the apparatus ensured completion of the project. He went beyond the call of duty to assist whenever and wherever possible and to provide advice and for this I cannot thank him enough.

- Mrs S. Warren, Secretary in the School of Physics, is thanked for all the help she provided. Her knowledge of Latex and willingness to assist with the typing of the tables in this thesis are really appreciated.

- The rest of the Physics staff, Mr. A. Zulu, Ms S. Khumalo, and Mrs B. Magubane are thanked for their assistance on various aspects of this project.

- My parents Dan and Segrie Chetty are my inspiration in life. A mention in this Acknowledgement section cannot fully express my deep love and appreciation for all that they have sacrificed for me in my pursuit of this degree. The monetary sacrifices they made over the years cannot ever be repaid. Without them this would never have been possible. My heartfelt appreciation and respect accompanies this message of thanks.

- My granny Logie Moodley and brother Indrasen Chetty are thanked as well: for always being there, and for listening to my "ups and downs" during this research. I must thank them also for the many sacrifices they made in helping me achieve my dreams.

- My late uncles Deena and Segran Moodley are acknowledged for the instrumental role they played in shaping me into the individual I am

today. In particular, my uncle Deena is remembered for instilling in me perserverance and the ambition to pursue a worthwhile goal. I am heartbroken that they cannot be here to share in my joy at this point.

- My late uncle Dan Naidoo deserves a mention here as well for his belief in my abilities. To my aunt Shamba, thanks for always supporting me in my endeavors.

- Mrs Robinna Singh and Ms Sanusha Naidoo are thanked for all their advice and motivation. Their support and assistance beyond the realm of this project are greatly appreciated. Mrs Singh is thanked, in particular, for her assistance at the onset of my university career.

- My late aunt and uncle, Joan and Trevor Moodley, are remembered for their words of encouragement and motivation.

- The NRF and DoL are thanked for their financial support, in the form of scholarships and bursaries, throughout this work. More especially, Joyce Mokoena at the NRF is thanked for ensuring the smooth administration of my scholarship.

- The NLC is acknowledged for their immense contribution to funding this project. In particular, Mr Thomas du Plooy is thanked for the efficient handling of all the project finances.

- Mr Karan Naidoo and Mrs Roshilla Singh, staff of the Student Funding Centre, are thanked for their roles in ensuring that my scholarship ap-

plications reached the designated centres on time and also for ensuring the prompt payment of money due to me.

- Mr Patrick Nair and Ms Michelle Govender, staff of the Student Fees office, are thanked for their prompt and efficient processing of my scholarship payments.

- To all those who have assisted me in various ways, and that I may have forgotten to mention, I apologise and thank you. Your assistance regardless of how big or small had a huge impact on the outcome of this project and it is acknowledged.

And last but certainly not least, I must thank the almighty Lord Shiva and Lord Hanuman for showering me with numerous blessing and keeping me safe and protected through many trying periods of my life. Mother Saraswathie is thanked for bestowing upon me the knowledge to complete this research.

Chapter 1

Introduction and theory

1.1 Introduction

It was in 1959 that Professor A. D. Buckingham revolutionised the way in which molecular electric quadrupole moments could be measured. He presented a theory [1] for an experiment that enabled the quadrupole moments of non-dipolar gas molecules with 3-fold or higher axial symmetry to be directly determined, from measurement of the birefringence induced in a low-pressure gas by an external electric field gradient. Prior to this innovation, all measurements of electric quadrupole moments were performed via indirect techniques, or specialised techniques suited to specific molecules, some of which will be discussed later in this chapter. The present work builds on and extends the work of Imrie [2] and Watson [3].

Debye [4] was the first to conceptualise the possibility of a birefringence in-

duced by an electric field gradient. He showed that this induced birefringence originates from the partial orientation of the molecular quadrupole moments by the field gradient, thereby causing the gas to become anisotropic. Measurement of this birefringence allows the molecular quadrupole moment of non-dipolar gas molecules with 3-fold or higher axial symmetry to be determined.

In 1963, Buckingham and Disch [5] were the first to assemble an apparatus for performing this experiment. Their apparatus allowed the first direct measurement of the quadrupole moment of carbon dioxide to be made. This measurement provided both the sign and magnitude of the quadrupole moment, and paved the way for experimental exploration of many other molecules, the quadrupole moments of which have since been determined.

The molar field-gradient-birefringence constant, or molar Buckingham constant, ${}_mQ$ is defined to be [6]

$$ {}_mQ = \frac{6n(3\epsilon_r + 2)}{5\epsilon_r(n^2+2)^2} lim_{E_{xx}\to 0} \left(\frac{n_x - n_y}{E_{xx}} \right) V_m \ , \tag{1.1} $$

where

- x, y, z refer to laboratory cartesian axes, with the z axis along the axis of the long cylindrical gas cell,

- $E_{xx} = \nabla_x E_x$ is the electric field gradient produced by two equally charged parallel wires lying in the yz plane within the earthed cell and equidistant from its axis,
- n_x and n_y are the refractive indices for a monochromatic light beam propagating along the axis of the cell and polarised parallel to the x and y axes respectively,
- n is the refractive index of the gas in the absence of the field gradient,
- ϵ_r is the relative permittivity of the gas in the absence of the field gradient, and
- V_m is the molar volume.

Because the anisotropy per molecule is increased by molecular interactions, the molar field-gradient-birefringence constant will not depend linearly on the gas density at higher pressures. Bearing this in mind, we can express ${}_mQ$ as a virial expansion

$$ {}_mQ = A_Q + \frac{B_Q}{V_m} + \frac{C_Q}{{V_m}^2} + \cdots , \tag{1.2} $$

where A_Q, B_Q and C_Q are the first, second and third electric-field-gradient-induced-birefringence virial coefficients respectively. In the above expression B_Q and C_Q describe the deviation of ${}_mQ$ from the ideal-gas value A_Q as a result of pair and triplet interactions respectively.

The molar Buckingham constant of the molecules studied in the present investigation did not exhibit any signs of density dependence over a range of pressure from 0.300 MPa to 2.600 MPa in preliminary studies on the gases thus allowing the approximation ${}_mQ = A_Q$ to be made with confidence.

1.2 Multipole moments

Although the charges in a molecule move, they generally do so at speeds very much less than the speed of light [7]. The electrostatic potential and field outside a molecule may be expressed in terms of electric multipole moments located at an arbitrary point inside the molecule. Also the interaction energy between two molecules depends in part on their on their respective multipole moments. Because of their role in intermolecular forces, electric multipoles have been used in attempts to explain the properties of imperfect gases, liquids, and solids.

Consider a distribution of charges q_i in a vacuum with displacements $\boldsymbol{r}_i$ from an arbitrary origin O. This origin is close to, or within, the charge distribution. The electrostatic potential at a point P with displacement $\boldsymbol{R}$ from O is

$$\phi(\mathbf{R}) = \frac{1}{4\pi\epsilon_0} \sum_i \frac{q_i}{|\mathbf{R} - \mathbf{r}_i|}. \tag{1.3}$$

The binomial theorem can now be used to expand the denominator in the above summation, provided that $R \geq r_i$. Thus we obtain

$$\phi(\mathbf{R}) = \frac{1}{4\pi\epsilon_0}\left[\frac{1}{R}\sum_i q_i + \frac{R_\alpha}{R^3}\sum_i q_i r_{i\alpha} + \frac{3R_\alpha R_\beta - R^2\delta_{\alpha\beta}}{2R^5}\sum_i q_i r_{i\alpha} r_{i\beta} + ...\right]. \tag{1.4}$$

Here, as in the remainder of this work, cartesian components are denoted by Greek subscripts. Repeated subscripts imply a summation over x, y and z, while the Kronecker delta tensor is indicated by $\delta_{\alpha\beta}$. Equation (1.4) can now be used to identify the various electric moments of the charge distribution as follows:

1. the total charge

$$q = \sum_i q_i, \tag{1.5}$$

2. the electric dipole moment

$$\mu_\alpha = \sum_i q_i r_{i\alpha}, \tag{1.6}$$

3. and the electric quadrupole moment

$$Q_{\alpha\beta} = \sum_i q_i r_{i\alpha} r_{i\beta}. \tag{1.7}$$

The definition of the quadrupole moment given in (1.7) is known as the primitive quadrupole moment. An alternative definition, which has come to be almost universally accepted, is the traceless quadrupole moment given by [8]

$$\Theta_{\alpha\beta} = \frac{1}{2}\left(3Q_{\alpha\beta} - Q_{\gamma\gamma}\delta_{\alpha\beta}\right) = \frac{1}{2}\sum_i q_i\left(3r_{i\alpha}r_{i\beta} - r_i^2\delta_{\alpha\beta}\right). \tag{1.8}$$

The potential in (1.4) can be written in terms of the defined moments of charge as

$$\phi(\mathbf{R}) = \frac{1}{R}q + \frac{R_\alpha}{R^3}\mu_\alpha + \frac{3R_\alpha R_\beta - R^2\delta_{\alpha\beta}}{2R^5}Q_{\alpha\beta} + \cdots. \tag{1.9}$$

This shows that successively higher multipole moments make contributions to the electrostatic potential that are successively smaller by a factor of order $\frac{1}{R}$. Thus moments such as the octopole, hexadecapole, $\cdots$, contribute much less to the potential of a quadrupolar molecule at a distant point and need not be considered in this investigation.

An electrostatic field $\boldsymbol{E}$ applied to a charge distribution produces a force $\boldsymbol{F}$ on it, which can be Taylor-expanded to give

$$F_\alpha = \sum_i q_i E_{i\alpha} = q(E_\alpha)_0 + \mu_\beta(\nabla_\beta E_\alpha)_0 + \frac{1}{2}Q_{\beta\gamma}(\nabla_\beta\nabla_\gamma E_\alpha)_0 + \cdots, \tag{1.10}$$

provided $\boldsymbol{E}$ does not vary too strongly over the distribution. The bracketed field derivatives in (1.10) are evaluated at the origin O at which the multipoles are located in the molecule. This equation can be used to show that a quadrupolar distribution will experience a torque in the region of a field gradient. Imrie and Raab [2, 9] showed that the potential energy of the charge distribution can be expressed as

$$U = -\int_{r_1(\mathbf{E}=\mathbf{0})}^{r_2(\mathbf{E}=\mathbf{E})} F_\alpha dr_\alpha = q\phi - \int_0^{\mathbf{E}} \mu_\alpha dE_\alpha - \frac{1}{3}\int_0^{\mathbf{E}} \Theta_{\alpha\beta} d(\nabla_\beta E_\alpha) - \cdots, \quad (1.11)$$

in which the traceless quadrupole moment in (1.8) is used.

For a rigid distribution - one not distorted by the field - (1.11) can be integrated to yield

$$U = q\phi - \mu^{(0)} E_\alpha - \frac{1}{3}\Theta^{(0)}_{\alpha\beta}\nabla_\alpha E_\beta. \quad (1.12)$$

Here the superscripted $^{(0)}$ on a moment indicates a permanent moment.

Since the quadrupole moment is a symmetric second-rank tensor, this can be specified relative to principal molecule-fixed axes, with the only non-zero components being Θ_{xx}, Θ_{yy}, and Θ_{zz}. Since from (1.8) we have $\Theta_{\alpha\alpha} = 0$, this means that only two components are independent, and these components will suffice in describing the interaction of a molecule with a field gradient.

If the molecule has a 3-fold or higher axial symmetry about its z-axis then

$$\Theta_{xx} = \Theta_{yy} = -\frac{1}{2}\Theta_{zz} \tag{1.13}$$

where Θ_{zz}, often denoted simply by Θ, is traditionally termed the quadrupole moment of the molecule [1].

We now determine the effect on the quadrupole moment of an arbitrary displacement of coordinate origin in a molecule. Let the origin be displaced by $\boldsymbol{d}$ from O to O'. Then the displacement of q_i from O' is $\boldsymbol{r}'_i = \boldsymbol{r}_i - \boldsymbol{d}$ and the quadrupole moment relative to O' is

$$\begin{aligned}\Theta'_{\alpha\beta} &= \frac{1}{2}\sum_i q_i \left(3r'_{i\alpha}r'_{i\beta} - (r'_i)^2\delta_{\alpha\beta}\right) \\ &= \Theta_{\alpha\beta} - \frac{3}{2}(\mu_\alpha r'_\beta + \mu_\beta r'_\alpha) + \mu_\gamma r'_\gamma \delta_{\alpha\beta} + \frac{1}{2}q\left\{(3r'_{i\alpha}r'_{i\beta} - (r'_i)^2\delta_{\alpha\beta}\right\}. \end{aligned} \tag{1.14}$$

From the above we see that if and only if the charge q and dipole moment μ are both zero, will the quadrupole moment be origin independent. Hence when we consider a dipolar molecule, the quadrupole moment will vary according to the choice of coordinate origin.

1.3 General electric-field-gradient-induced birefringence (EFGIB) theory

Equation (1.12) suggests that the quadrupole moment of a molecule may be measured through the change in energy when a known field gradient is applied to the molecule. This seems simple enough, and should produce a very accurate result for the quadrupole moment of a molecule. However, to produce a field gradient sufficiently large to cover molecular dimensions is extremely difficult, and this method is not feasible within the experimental limits of modern science.

The solution to this impracticality was first proposed by Buckingham [1] in 1959. It is a method very similar to that presented by Buckingham and Pople for the Kerr effect [10] and the Cotton-Mouton effect [11] and provides a unique but elegant variation to the idea proposed above. The strength of the electric field gradient required by this method is readily achievable in the laboratory, and so accurate measuremnts of the electric quadrupole moment of the molecule become feasible. Nevertheless, it is a fairly complex experiment, the details of which are outlined below.

Gas molecules having a permanent quadrupole moment are contained in a cell [1], and a uniform electric field gradient is produced along the cell axis. The field gradient partially orients the molecules, this orientation resulting

from the torque exerted by the field gradient on each molecule's quadrupole moment. As a result the gas becomes anisotropic, and hence exhibits birefringence. This is termed induced birefringence, since the applied field is responsible for creating it. Measurement of this induced birefringence yields the molar Buckingham constant ${}_mQ$, and hence, via suitable molecular-tensor theory, the electric quadrupole moment.

The leading moment of charge is the only one independent of origin [1]. Consequently, the quadrupole moment of a dipolar molecule must necessarily depend on origin. Buckingham and Longuet-Higgins [12] and later Imrie and Raab [9] discussed, in different theories of the Buckingham effect, the location of an appropriate origin in dipolar molecules. Because of discordant results Raab and de Lange revisited the theory and showed that the two approaches could be reconciled by correcting mathematical defects in both [13, 14], confirming the Buckingham and Longuet-Higgins result. Measurements of the quadrupole moment of several dipolar molecules have been achieved through this method, the first being by Buckingham, Disch and Dunmur [15], followed by various others [2, 3, 16, 17].

1.3.1 Non-dipolar molecules

The method used in the following analysis is based on the approach of Buckingham [1]. Consider a neutral molecule having configuration τ in an external electrostatic field E and field gradient ∇E. The energy of this molecule can be written as

$$\begin{aligned} U(\tau, E, \nabla E) &= U^{(0)} - \mu_\alpha E_\alpha - \frac{1}{2}\alpha_{\alpha\beta}E_\alpha E_\beta - \frac{1}{6}\beta_{\alpha\beta\gamma}E_\alpha E_\beta E_\gamma \\ &- \frac{1}{3}\Theta_{\alpha\beta}E_{\alpha\beta} - \frac{1}{3}A_{\alpha\beta\gamma}E_\alpha E_{\beta\gamma} - \frac{1}{6}B_{\alpha\beta\gamma\delta}E_\alpha E_\beta E_{\gamma\delta} - \cdots \end{aligned} \tag{1.15}$$

where, along the axis of the two-wire field-gradient cell, $E_\alpha = 0$ and

$$\nabla_\alpha E_\beta = E_{\alpha\beta} = \begin{pmatrix} E_{xx} & 0 & 0 \\ 0 & E_{yy} = -E_{xx} & 0 \\ 0 & 0 & 0 \end{pmatrix}. \tag{1.16}$$

In the above, μ_α and $\Theta_{\alpha\beta}$ represent the permanent dipole and quadrupole moments, respectively. The higher rank tensors $A_{\alpha\beta\gamma}$ and $B_{\alpha\beta\gamma\delta}$ are the polarisabilities which describe the distortion of the molecule as a result of the field E_α and field gradient $E_{\alpha\beta}$.

The anisotropy in the refractive index, $n_x - n_y$, of a gas for a beam of light travelling along the axis of the cell with electric vectors in the x and y

direction is

$$n_x - n_y = \frac{N_A \bar{\Pi}}{2\epsilon_0 V_m} \tag{1.17}$$

where

- N_A is Avogadro's number,
- ϵ_0 is the permittivity of free space,
- V_m is the molar volume, and
- $\bar{\Pi}$ is the average over all configurations of the quantity $\Pi(\tau, E, \nabla E) = \Pi_{\alpha\beta}\left(a_\alpha^x a_\beta^x - a_\alpha^y a_\beta^y\right)$, in which a_α^x is the direction cosine between the x space-fixed and α molecule-fixed axes, and a_α^y between the y space-fixed and α molecule-fixed axes.

The differential polarisability $\Pi_{\alpha\beta}$ is defined to be the increase in dipole moment per unit increase in field, so that

$$\Pi_{\alpha\beta} = -\frac{\partial \mu_\alpha}{\partial E_\beta} = -\frac{\partial^2 U(\tau, E, \nabla E)}{\partial E_\alpha \partial E_\beta}. \tag{1.18}$$

From equations (1.15) and (1.18) we obtain

$$\Pi_{\alpha\beta} = \alpha_{\alpha\beta} + \beta_{\alpha\beta\gamma} E_\gamma + \frac{1}{3} B_{\alpha\beta\gamma\delta} E_{\gamma\delta} + \cdots . \tag{1.19}$$

Since the molecule is in fact tumbling in space, the differential polarisability has to be averaged over all possible configurations in the presence of the

biasing influences of the applied field and field gradient. The period of oscillation of the light wave is assumed to be much smaller than the rotation time of the molecule. It is further assumed that the rotational energy levels are sufficiently close for the orientation of the molecule to be regarded as effectively continuous, and so we can average over configurations using a Boltzmann-type weighting factor [1]. We write

$$\bar{\Pi} = \frac{\int \Pi(\tau, E, \nabla E)\ e^{-U(\tau,E,\nabla E)/kT}\ d\tau}{\int e^{-U(\tau,E,\nabla E)/kT}\ d\tau}. \tag{1.20}$$

To convert the biased average in equation (1.20) into an isotropic average, we Taylor expand $\bar{\Pi}$ in powers of field and field gradient while bearing in mind that it depends on the field and field gradient both through $\Pi(\tau, E, \nabla E)$ and through the energy $U(\tau, E, \nabla E)$. Thus

$$\bar{\Pi} = A\ E_{xx} + B\ E^2 + C\ E_{xx}^3 + \cdots \tag{1.21}$$

where the coefficients are

$$A = \left[\frac{\partial \bar{\Pi}}{\partial E_{xx}}\right]_{E_{xx}=0}, \tag{1.22}$$

$$B = \frac{1}{2}\left[\frac{\partial^2 \bar{\Pi}}{\partial E^2}\right]_{E=0}, \tag{1.23}$$

and

$$C = \frac{1}{6}\left[\frac{\partial^3 \bar{\Pi}}{\partial E_{xx}^3}\right]_{E_{xx}=0}. \tag{1.24}$$

$\bar{\Pi}$ is an even function of the electric field and an odd one in the electric field gradient. The coefficient of E^2 leads to the Kerr constant, but in the two-wire field-gradient cell, $E = 0$ on the z axis. Provided the electric field gradient is not too large, i.e. $E_{xx} < 10^9\ \mathrm{V\,m^{-2}}$, the first term in E_{xx} will suffice to describe the anisotropy induced in the gas. We have

$$\bar{\Pi} = \left[\frac{\partial \bar{\Pi}}{\partial E_{xx}}\right]_{E_{xx}=0} E_{xx}. \tag{1.25}$$

Performing the differentiation on equation (1.20), we can obtain an expression for $\bar{\Pi}$ in the case of moderate electric field gradients.

$$\bar{\Pi} = \left\{\left\langle \frac{\partial \Pi}{\partial E_{xx}} \right\rangle - \frac{1}{kT}\left\langle \Pi \frac{\partial U}{\partial E_{xx}} \right\rangle\right\} E_{xx} \tag{1.26}$$

where the angular brackets represent an isotropic average over all possible orientations τ when the electric field gradient $E_{xx} = 0$.

Now

$$\left(\frac{\partial \Pi}{\partial E_{xx}}\right)_{E_{xx}=0} = \frac{\partial}{\partial E_{xx}}\left(\Pi_{\alpha\beta}\left(a_\alpha^x a_\beta^x - a_\alpha^y a_\beta^y\right)\right)_{E_{xx}=0}. \tag{1.27}$$

Substituting the expression for $\Pi_{\alpha\beta}$ in (1.19) into equation (1.27) yields

$$\left(\frac{\partial \Pi}{\partial E_{xx}}\right)_{E_{xx}=0} = \left[\frac{\partial}{\partial E_{xx}}\left(\alpha_{\alpha\beta} + \beta_{\alpha\beta\gamma}E_\gamma + \frac{1}{3}B_{\alpha\beta\gamma\delta}E_{\gamma\delta}\right)\left(a_\alpha^x a_\beta^x - a_\alpha^y a_\beta^y\right)\right]_{E_{xx}=0}. \tag{1.28}$$

The electric field gradient $E_{\gamma\delta}$ in equation (1.28) may be written as

$$E_{\gamma\delta} = \left(a_\gamma^x a_\delta^x - a_\gamma^y a_\delta^y\right) E_{xx} \tag{1.29}$$

so that

$$\left(\frac{\partial \Pi}{\partial E_{xx}}\right)_{E_{xx}=0} = \left[\frac{\partial}{\partial E_{xx}}\left\{\alpha_{\alpha\beta} + \beta_{\alpha\beta\gamma}E_\gamma + \frac{1}{3}B_{\alpha\beta\gamma\delta}\left(a_\gamma^x a_\delta^x - a_\gamma^y a_\delta^y\right)E_{xx}\right\}\left(a_\alpha^x a_\beta^x - a_\alpha^y a_\beta^y\right)\right]_{E_{xx}=0}. \tag{1.30}$$

Hence we obtain

$$\left\langle \frac{\partial \Pi}{\partial E_{xx}} \right\rangle = \frac{1}{3}B_{\alpha\beta\gamma\delta}\left\langle \left(a_\gamma^x a_\delta^x - a_\gamma^y a_\delta^y\right)\left(a_\alpha^x a_\beta^x - a_\alpha^y a_\beta^y\right)\right\rangle. \tag{1.31}$$

Using the FOIL rule for multiplication [18], we can expand the brackets to obtain

$$\left\langle \frac{\partial \Pi}{\partial E_{xx}} \right\rangle = \frac{1}{3}B_{\alpha\beta\gamma\delta}\left\langle a_\alpha^x a_\beta^x a_\gamma^x a_\delta^x - a_\alpha^y a_\beta^y a_\gamma^x a_\delta^x - a_\alpha^x a_\beta^x a_\gamma^y a_\delta^y + a_\alpha^y a_\beta^y a_\gamma^y a_\delta^y\right\rangle. \tag{1.32}$$

The terms in equation (1.32) can be evaluated by appealing to the standard results for isotropic averages as given in [1, 10, 19], where it is shown that

$$\left\langle a_\alpha^x a_\beta^x a_\gamma^x a_\delta^x \right\rangle = \frac{1}{15}\left(\delta_{\alpha\beta}\delta_{\gamma\delta} + \delta_{\alpha\gamma}\delta_{\beta\delta} + \delta_{\alpha\delta}\delta_{\beta\gamma}\right) \tag{1.33}$$

and

$$\left\langle a_\alpha^y a_\beta^y a_\gamma^x a_\delta^x \right\rangle = \frac{1}{30}\left(4\delta_{\alpha\beta}\delta_{\gamma\delta} - \delta_{\alpha\gamma}\delta_{\beta\delta} - \delta_{\alpha\delta}\delta_{\beta\gamma}\right). \tag{1.34}$$

Since $\left\langle a_\alpha^x a_\beta^x a_\gamma^x a_\delta^x \right\rangle = \left\langle a_\alpha^y a_\beta^y a_\gamma^y a_\delta^y \right\rangle$ and $\left\langle a_\alpha^y a_\beta^y a_\gamma^x a_\delta^x \right\rangle = \left\langle a_\alpha^x a_\beta^x a_\gamma^y a_\delta^y \right\rangle$, we simplify equation (1.32) to obtain

$$\left\langle \frac{\partial \Pi}{\partial E_{xx}} \right\rangle = \frac{1}{3} B_{\alpha\beta\gamma\delta} \left(\frac{2}{30}\right) \left(-2\delta_{\alpha\beta}\delta_{\gamma\delta} + 3\delta_{\alpha\gamma}\delta_{\beta\delta} + 3\delta_{\alpha\delta}\delta_{\beta\gamma}\right) \tag{1.35}$$

which reduces to

$$\left\langle \frac{\partial \Pi}{\partial E_{xx}} \right\rangle = \frac{2}{90}\left(-2B_{\beta\beta\gamma\gamma} + 3B_{\alpha\beta\alpha\beta} + 3B_{\alpha\beta\beta\alpha}\right). \tag{1.36}$$

Here $B_{\beta\beta\gamma\gamma} = 0$ since the B-tensor is traceless. Furthermore, $B_{\alpha\beta\alpha\beta} = B_{\alpha\beta\beta\alpha}$ so that equation (1.36) yields

$$\left\langle \frac{\partial \Pi}{\partial E_{xx}} \right\rangle = \frac{2}{90}\left(6\, B_{\alpha\beta\alpha\beta}\right) = \frac{2}{15} B_{\alpha\beta\alpha\beta}. \tag{1.37}$$

We can now proceed to solve for the second term in equation (1.26).

$$\left(\Pi\frac{\partial U}{\partial E_{xx}}\right)_{E_{xx}=0} = \left[\left(\alpha_{\alpha\beta} + \frac{1}{3}B_{\alpha\beta\gamma\delta}E_{\gamma\delta} + ...\right)\left(a^x_\alpha a^x_\beta - a^y_\alpha a^y_\beta\right)\left(\frac{\partial U}{\partial E_{xx}}\right)\right]_{E_{xx}=0} \tag{1.38}$$

where $\left(\frac{\partial U}{\partial E_{xx}}\right)_{E_{xx}=0}$ is easily obtained from differentiating equation (1.15) with respect to the electric field gradient, yielding

$$\left(\frac{\partial U}{\partial E_{xx}}\right)_{E_{xx}=0} = -\frac{1}{3}\,\Theta_{\gamma\delta}\left(a^x_\gamma a^x_\delta - a^y_\gamma a^y_\delta\right). \tag{1.39}$$

We have

$$\left\langle \Pi\frac{\partial U}{\partial E_{xx}}\right\rangle = -\frac{1}{3}\,\alpha_{\alpha\beta}\,\Theta_{\gamma\delta}\left\langle\left(a^x_\alpha a^x_\beta - a^y_\alpha a^y_\beta\right)\left(a^x_\gamma a^x_\delta - a^y_\gamma a^y_\delta\right)\right\rangle, \tag{1.40}$$

so that

$$\begin{aligned}\left\langle \Pi\frac{\partial U}{\partial E_{xx}}\right\rangle &= -\frac{1}{3}\,\alpha_{\alpha\beta}\,\Theta_{\gamma\delta}\,\frac{2}{30}\left(-2\delta_{\alpha\beta}\delta_{\gamma\delta} + 3\delta_{\alpha\gamma}\delta_{\beta\delta} + 3\delta_{\alpha\delta}\delta_{\beta\gamma}\right)\\ &= -\frac{2}{90}\left(-2\alpha_{\alpha\alpha}\Theta_{\gamma\gamma} + 3\alpha_{\alpha\beta}\Theta_{\alpha\beta} + 3\alpha_{\alpha\beta}\Theta_{\beta\alpha}\right).\end{aligned} \tag{1.41}$$

In equation (1.41), the term $\alpha_{\alpha\alpha}\Theta_{\gamma\gamma} = 0$ since the quadrupole tensor is traceless, and so

$$\left\langle \Pi \frac{\partial U}{\partial E_{xx}} \right\rangle = -\frac{2}{15}\ \alpha_{\alpha\beta}\ \Theta_{\alpha\beta}. \tag{1.42}$$

Substituting equations (1.42) and (1.37) into equation (1.26) we obtain

$$\bar{\Pi} = \left\{ \left\langle \frac{\partial \Pi}{\partial E_{xx}} \right\rangle - \frac{1}{kT} \left\langle \Pi \frac{\partial U}{\partial E_{xx}} \right\rangle \right\} E_{xx} = \frac{2}{15} \left[B_{\alpha\beta\alpha\beta} + \ \frac{\alpha_{\alpha\beta}\ \Theta_{\alpha\beta}}{kT} \right] E_{xx}. \tag{1.43}$$

We can now substitute equation (1.43) into equation (1.17) to obtain an expression for the induced birefringence.

$$\begin{aligned} n_x - n_y &= \frac{N_A \bar{\Pi}}{2\epsilon_0 V_m} \\ &= \frac{N_A}{2\epsilon_0 V_m} \frac{6}{45} \left[B_{\alpha\beta\alpha\beta} + \ \frac{\alpha_{\alpha\beta}\ \Theta_{\alpha\beta}}{kT} \right] E_{xx} \\ &= \frac{N_A E_{xx}}{15\epsilon_0 V_m} \left[B_{\alpha\beta\alpha\beta} + \ \frac{\alpha_{\alpha\beta}\ \Theta_{\alpha\beta}}{kT} \right]. \end{aligned} \tag{1.44}$$

Equation (1.44) above is the classical formula for the induced birefringence. EFGIB experiments measure the molar Buckingham constant ${}_mQ$, which is analogous to the molar constants for the Kerr and Cotton-Mouton effects. At typical pressures used in the experimental part of this work, we make the approximation $n = 1$ since this affects ${}_mQ$ by never more than 0.4%. The contribution from ϵ_r, however, can still be as much as a few percent, and may not be neglected. The Buckingham constant in (1.1) becomes

$$ {}_mQ = \frac{2\left(3\epsilon_r + 2\right)}{15\epsilon_r} \frac{\left(n_x - n_y\right)}{E_{xx}} V_m, \tag{1.45} $$

where the electric field gradient is relatively weak. And so, using (1.44) in (1.45) we obtain, for the special case of axially-symmetric molecules,

$$ {}_mQ = \frac{2\left(3\epsilon_r + 2\right) N_A}{225\epsilon_r\epsilon_0} \left[\frac{15}{2}B + \frac{\Delta\alpha\,\Theta}{kT}\right]. \tag{1.46} $$

Here we have written

- $B_{\alpha\beta\alpha\beta} - \beta_{\alpha\beta\alpha\beta} - \frac{5}{\omega}\epsilon_{\alpha\beta\gamma}J_{\alpha\beta\gamma}$ as $\frac{15}{2}B$. $\epsilon_{\alpha\beta\gamma}$ is the alternating tensor and ω is the angular frequency of the light. The hyperpolarisabiliy tensors $B_{\alpha\beta\alpha\beta}$, $\beta_{\alpha\beta\alpha\beta}$, and $J_{\alpha\beta\gamma}$ are defined elsewhere [12], and
- $\Delta\alpha = \alpha_{zz} - \alpha_{xx}$ [20].

1.3.2 Quantum corrections

In the above classical analysis it was assumed that $\bar{\Pi}$ and U are continuous functions over the orientational coordinates of the molecule. If we now consider the effects of quantisation on the rotational motion of the molecule, $\bar{\Pi}$ and U are no longer continuous and the use of Boltzmann statistics as in (1.20) is no longer valid. Instead, quantum-mechanical averaging techniques need to be applied. Buckingham and Pariseau [21] were the first to show that under quantum-mechanical conditions $\bar{\Pi}$ becomes

$$\bar{\Pi} = \frac{\sum_i \left\langle \varphi^{(i)} | \Pi | \varphi^{(i)} \right\rangle \; e^{-U^{(i)}/(kT)}}{\sum_i e^{-U^{(i)}/(kT)}} \tag{1.47}$$

where $\varphi^{(i)}$ and $U^{(i)}$ are the wavefunction and energy respectively of the i^{th} state of the molecule perturbed by the electric field gradient.

The electric-field-gradient-induced birefringence is now [21]

$$n_x - n_y = \frac{(3\epsilon_r + 2)\, N_A E_{xx}}{75\epsilon_r \epsilon_0 V_m} \left[B'_{\alpha\beta\alpha\beta} + \; \frac{\alpha_{\alpha\beta}\, \Theta_{\alpha\beta}}{kT} f(T) \right], \tag{1.48}$$

where $B'_{\alpha\beta\alpha\beta}$ differs slightly from $B_{\alpha\beta\alpha\beta}$ due to centrifugal distortion, and where

$$f(T) = 1 - \left[\frac{\hbar^2}{2kTI} \right] + \frac{8}{15} \left[\frac{\hbar^2}{2kTI} \right]^2 - \cdots \tag{1.49}$$

for an axially-symmetric molecule, where I is its principal moment of inertia.

This correction is imperative in the study of the hydrogen molecule and the quantum corrections for the various temperatures are shown in Chapter 4. The moments of inertia used to calculate $f(T)$ in this work were obtained from Moore [22].

1.3.3 Dipolar molecules

Buckingham and Longuet-Higgins [12] have derived an expression for the EFGIB $n_x - n_y$ in a low-pressure gas of dipolar molecules, obtaining for axially-symmetric molecules

$$n_x - n_y = \frac{(3\epsilon_r + 2)\, N_A E_{xx}}{75\epsilon_r \epsilon_0 V_m} \left\{ \frac{15}{2} B + \frac{1}{kT} \left[\Delta\alpha\, \Theta - \mu \left(A_{||} + 2A_{\perp} + \frac{10}{\omega} G' \right) \right] \right\} \tag{1.50}$$

where

- N_A is Avogadro's constant,
- B is a grouping of molecular hyperpolarisabilities, defined in [12],
- $\Delta\alpha$ is the optical-frequency anisotropy in the polarisability [23],
- μ is the electric dipole moment,
- A and G are the higher optical-frequency polarisabilities which describe the electric dipole induced by the field gradient, and the oscillating magnetic field associated with the light wave, respectively [12], and

- ω is the angular frequency of the light.

Substitution of equation (1.50) into equation (1.45) yields an expression for the molar Buckingham constant

$$ {}_mQ = \frac{2\left(3\epsilon_r + 2\right) N_A}{225\epsilon_r\epsilon_0}\left\{\frac{15}{2}B + \frac{1}{kT}\left[\Delta\alpha\Theta - \mu\left(A_{||} + 2A_{\perp} + \frac{10}{\omega}G'\right)\right]\right\}. \tag{1.51} $$

Since only the leading moment of charge is origin independent [8], the quadrupole moment of a dipolar molecule depends on the origin to which it is referred. Buckingham and Longuet-Higgins [12] defined the quadrupole moment relative to a point called the effective quadrupole centre (EQC), where $(A_{||} + 2A_{\perp} + \frac{10}{\omega}G') = 0$. The EQC is not the centre of mass (CM) of the molecule, and since other experiments (see the following section) determine $\Theta_{\mathtt{CM}}$, caution must be excercised (in the case of dipolar molecules) when comparing quadrupole moments $\Theta_{\mathtt{EQC}}$ determined by EFGIB experiments with $\Theta_{\mathtt{CM}}$ values determined either by *ab initio* computation or other experiments. For axially-symmetric molecules, both the EQC and the CM lie on the molecular axis of rotational symmetry (the $z-$axis), and it is possible to show that the quadrupole moments referred to these two different origins are related via [12]

$$ \Theta_{\mathtt{CM}} - \Theta_{\mathtt{EQC}} = 2R\mu_z \tag{1.52} $$

where μ_z is the electric dipole moment of the molecule, and R is the distance from the CM to the EQC.

1.4 Other methods of determining quadrupole moments

1.4.1 The anisotropic magnetic susceptibilty method

Towards the latter part of the sixties, microwave spectroscopy was used by Flygare and Benson [24] to measure the molecular Zeeman effect. This technique also provided an accurate, albeit indirect, means of measuring the molecular quadrupole moment. This method is briefly outlined below.

A freely rotating molecule with zero orbital and spin-electronic angular momentum in the ground electronic state which interacts with an external magnetic field, gives rise to the rotational Zeeman effect. The strongest of these interactions involves the molecular magnetic dipole moment tensor or g-value and gives rise to what is termed the first-order Zeeman effect. Weaker interactions give rise to higher-order Zeeman effects. The response of the electrons in the molecule to the external magnetic field produces the second-order Zeeman effect, from which the anisotropy in the magnetic susceptibility $\Delta\chi$ can be measured. If the molecular g-value and the magnetic anisotropy are known, then this leads to an experimental determination of the diagonal elements of the molecular quadrupole moment tensor. This tensor is in the principal inertial axis system of the molecule, and the value of Θ is given relative to the centre of mass $\Theta_{\mathtt{CM}}$.

Flygare [25] extended this approach to produce an expression for the molecular quadrupole moment of a planar axially-symmetric molecule, namely

$$\Theta = \frac{-e}{M}\left(g_{||}I_{||} - g_{\perp}I_{\perp}\right) - \frac{4m}{e}\Delta\chi\,, \tag{1.53}$$

where $\Delta\chi = \chi_{||} - \chi_{\perp}$ is the magnetic anisotropy, $I_{||}$ and $I_{\perp}$ are the principal moments of inertia parallel and perpendicular to the principal axis, M is the mass of the proton, m the electronic mass, e is the elementary charge and $g_{\perp}$ and $g_{||}$ are the molecular magnetic dipole moments parallel and perpendicular to the principal axis.

Hüttner and Flygare [26] showed that for a linear molecule (1.53) reduces to

$$\Theta = \frac{eg_{\perp}I_{\perp}}{M} - \frac{4m}{e}\Delta\chi. \tag{1.54}$$

The measurement of molecular g-tensors and magnetic susceptibilities is an important field of experimental work, but it has an added advantage in that it also allows for the molecular quadrupole moment to be determined in both sign and magnitude.

For smaller molecules the quadrupole moment obtained in this manner is fairly accurate. However, for larger molecules the quadrupole moment ob-

tained through this method is unreliable, mainly due to the fact that the terms involving $\Delta\chi$ and $g_\perp$ increase with molecular size. This results in a small difference between the two terms, giving rise to a relatively large uncertainty in Θ. An example is that of carbon dioxide for which Gustafson and Gordy [27] demonstrated the shortcoming of this method.

Nevertheless, the magnetic-anisotropy method still has value. Levy [28] showed that this method has a feature, unavailable in the induced-birefringence technique, in that it allows a number of components of the quadrupole moment to be determined, rather than just a single value.

1.4.2 The second virial-coefficient method

Interactions between gas molecules result in deviations from ideal gas behavior. The deviation from the ideal gas law is given by

$$\frac{P\,V_m}{R\,T} = 1 + \frac{B(T)}{V_m} + \frac{C(T)}{V_m^2} + \cdots , \tag{1.55}$$

where $B(T)$ and $C(T)$ are the second and third pressure virial coefficients respectively, and are functions only of the temperature of the gas.

The leading molecular quantity in the statistical-mechanical expression for

$B(T)$ for non-dipolar molecules is the electric quadrupole moment [29]. However, because of other contributions to *B(T)* and assumptions in the theory, this method does not yield values for the electric quadrupole moment as accurate as those obtained from the Buckingham effect. Prior to the advent of the Buckingham theory Bose and co-workers used $B(T)$ data to determine the quadrupole moments of a variety of molecules [29-33].

1.4.3 Collision-induced absorption

This technique was described by Buckingham [8], and has been used to measure quadrupole moments by a number of researchers [34-37]. As with all indirect techniques, results for this method are dependent on the model chosen for the description of the interaction potential. Some workers have succeeded in obtaining results which agree reasonably well with those obtained via induced birefringence [39, 40]; however the precision of reported values is often not better than 10%, whereas the results from the induced-birefringence experiment provide results of far greater accuracy.

The principle of this method is quite simple. A non-dipolar molecule can acquire a dipole moment induced at elevated pressures by intermolecular forces, which act within clusters of two or more molecules. These induced dipole moments result from short-range overlap forces and the resultant polarisation of one molecule by the quadrupole field of the other. Induced vibrational, rotational, and translational transitions hence also arise, which

can be studied using infrared absorption.

From these spectra, an absorption coefficient can be experimentally determined. The expansion of this coefficient as a function of density [35] yields the coefficients of rotational-translation absorption between pairs and triplets of molecules. From the assumptions that the contribution to the induced dipole moment arises from the quadrupole induction and that the overlap forces are negligible, the quadrupole moment can be obtained [37, 38].

1.4.4 Ion-molecule scattering experiments

A different approach was considered by Budenholzer *et al.* [41], and entailed calculating the quadrupole moment from data obtained via ion-molecule scattering experiments. These appear to be the only researchers who attempted to determine the quadrupole moment in this fashion. In their work, both theoretical and experimental, they investigated the scattering of low-energy ions off various molecules. From this the molecular cross-sections were calculated.

The scattering of low-energy particles is primarily determined by the long-range potential. For the molecules chosen, these potentials were quadrupolar in nature. The values reported for nitrogen and carbon dioxide are in good agreement with those obtained from the induced-birefringence experiment. However, the precision of their results is limited to only two significant figures.

1.4.5 Nuclear spin relaxation

The results obtained for the quadrupole moment using nuclear spin relaxation times are obtained using a number of approximations in theory. Nevertheless they are in very good agreement with those obtained via the induced-birefringence experiment. Bloom *et al.* [42] have done extensive work in this field for a series of simple gas molecules.

1.5 Discussion

The induced-birefringence experiment is currently the only direct means of determining molecular electric quadrupole moments of independent gas molecules. It is also the most accurate means of all the methods discussed above. However, the above methods can be useful in determining quadrupole moments in cases were the induced-birefringence experiment fails to give reliable results, mainly where the effect is small. Some of these methods can also provide other information about the quadrupole moment tensor, such as in the case of the magnetic anisotropy method.

The measurable effect from the induced-birefringence technique is very small when compared to other birefringence experiments such as the Cotton-Mouton or the Kerr effects. To ensure that definitive results for the molecular electric quadrupole moment are obtained it is necessary to perform the experiment over a range of temperature. This is done in order to separate the

term in (1.46) in which Θ appears from the temperature-independent term which contains the quadrupole hyperpolarisability. The experiment becomes increasingly difficult to perform as the temperature increases since the relevant term is inversely proportional to the temperature.

The intention of the present research was to develop and use an apparatus to measure the quadrupole moments of molecular gases using the Buckingham effect. This has been achieved and measurements of carbon dioxide, nitrous oxide, carbon monoxide, carbonyl sulphide, and hydrogen are reported in this work. The results, over a range of temperature for all gases except carbonyl sulphide, are presented in Chapter 4.

Bibliography

[1] A. D. Buckingham, *J. Chem. Phys.,* **30**, 1580 (1959)

[2] D. A. Imrie, *PhD Thesis, University of Natal (Pietermaritzburg)* (1993)

[3] J. N. Watson, *PhD Thesis, University of New England* (1994)

[4] P. Debye, *Phys. Z.,* **22**, 302 (1921)

[5] A. D. Buckingham and R. L. Disch, *Proc. Roy. Soc. A,* **273**, 275 (1963)

[6] J. Vrbancich and G. L. D. Ritchie, *J. Chem. Soc. Faraday Trans II,* **76**, 648 (1980)

[7] E. Hecht and A. Zajac, 1979, *Optics,* Addison-Wesley Publishing Company

[8] A. D. Buckingham, *Quart. Rev.,* **13**, 183 (1959)

[9] D. A. Imrie and R. E. Raab , *Molec. Phys.,* **74**, 833 (1991)

[10] A. D. Buckingham and J. A. Pople, *Proc. Phys. Soc.,* **68A**, 905 (1955)

[11] A. D. Buckingham and J. A. Pople, *Proc. Phys. Soc.,* **69B**, 1133 (1956)

[12] A. D. Buckhingham and H. C. Longuet-Higgins, *Molec. Phys.,* **14**, 63 (1968)

[13] R. E. Raab and O. L. de Lange , *Molec. Phys.,* **101**, 3467 (2003)

[14] O. L. de Lange and R. E. Raab, *Molec. Phys.,* **102**, 125 (2004)

[15] A. D. Buckingham, R. L. Disch, and D. A. Dunmur, *J. Amer. Chem. Soc.,* **90**, 3104 (1968)

[16] A. D. Buckingham, C. Graham, and J. H. Williams, *Molec. Phys.,* **49**, 703 (1983)

[17] C. Graham, J. Pierrus, and R. E. Raab, *Molec. Phys.,* **67**, 9939 (1989)

[18] R. Steege and K. Bailey, *Schaum's Outline of Theory and Problems of Intermediate Algebra* (New York: McGrawHill) (1997)

[19] A. L. Andrews and A. D. Buckingham, *Molec. Phys.,* **3**, 183 (1960)

[20] A. D. Buckingham, *Adv. Chem. Phys.,* **12**, 107 (1967)

[21] A. D. Buckingham and M. Pariseau, *Trans. Far. Soc.,* **62**, 1 (1966)

[22] W. J. Moore, *Physical Chemistry,* 5th edition (Longman) (1972)

[23] M. P. Bogaard, A. D. Buckingham, R. K. Pierens, and A. H. White, *Trans. Faraday Soc.,* **74**, 3008 (1978)

[24] W. H. Flygare and R. C. Benson, *Molec. Phys.,* **20**, 225 (1971)

[25] W. H. Flygare, *Chem. Rev.,* **74**, 653 (1974)

[26] W. Hüttner and W. H. Flygare, *J. Chem. Phys.,* **47**, 4137 (1967)

[27] S. Gustafson and W. Gordy, *J. Chem. Phys.,* **52**, 579 (1970)

[28] D. H. Levy, *J. Chem. Phys.,* **48**, 5026 (1968)

[29] V. P. Krishnaji, *Rev. Mod. Phys.,* **38**, 690 (1966)

[30] T. K. Bose and R. H. Cole, *J. Chem. Phys.,* **52**, 140 (1970)

[31] T. K. Bose and R. H. Cole, *J. Chem. Phys.,* **54**, 3829 (1971)

[32] S. Kirouac and T. K. Bose, *J. Chem. Phys.,* **59**, 3043 (1973)

[33] J. M. St-Arnaud and T. K. Bose, *J. Chem. Phys.,* **68**, 2129 (1978)

[34] T. K. Bose, K. Boudjarane, J. Hout, and J. M. St-Arnaud, *J. Chem. Phys.,* **89**, 7435 (1988)

[35] J. D. Poll and J. Van Kranendonk, *Can. J. Phys.,* **39**, 189 (1961)

[36] W. Ho, G. Birnbaum and A. Rosenberg, *J. Chem. Phys.,* **55**, 1028 (1971)

[37] A. Rastogi and R. P. Lowndes, *J. Phys. B.,* **10**, 495 (1977)

[38] I. R. Dagg, W. Smith L. A. A. Read, *Can. J. Phys.,* **60**, 16 (1982)

[39] T. G. Copeland and R. H. Cole, *Chem. Phys. Lett.,* **21**, 289 (1973)

[40] U. Buontempo, S. Cunsolo, and G. Jacucci, *J. Chem. Phys.,* **59**, 3750 (1973)

[41] F. E. Budenholzer, E. A. Gislason, A. D. Jorgenson, and J. Grobe, *Chem. Phys. Lett.,* **47**, 429 (1977)

[42] M. Bloom, I. Oppenheim, M. Lipsicas, C. G. Wade, and C. F. Yarnell, *J. Chem. Phys.,* **43**, 1036 (1965)

Chapter 2

Preliminaries to the EFGIB experiment

2.1 Introduction

In this chapter, we quote the relevant results of the Jones calculus to determine the intensity of the light reaching the detector. In addition, the apparatus used in the experiment is introduced and briefly discussed together with possible sources of error and their contribution to the systematic error of the experimental results.

2.2 The Jones Calculus

Imrie [1] provides a comprehensive study of the Jones calculus in general as well as its application in determining the intensity of the light reaching

the detector in the EFGIB experiment. In this section, a summary of the relevant results is made.

2.2.1 The Jones calculus for the EFGIB experiment

The optical components in the train between crossed polariser and analyser are shown in Figure 2.1. Pierrus [2] suggested that the windows of the gas

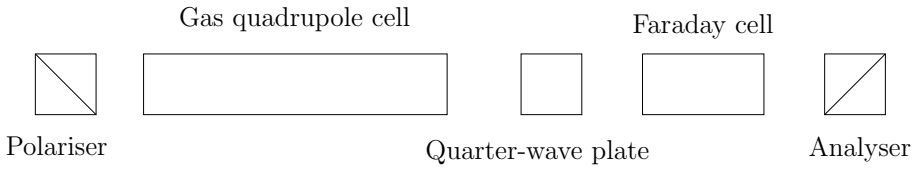

Figure 2.1: The optical train

quadrupole cell must be included in the optical train since they may impact on the results of the experiment due to the birefringences that may exist in them. These birefringences can only result from the mechanical clamping of the windows into the housing mechanisms, since the windows are cut from high-quality low-strain Pockels glass to minimise strain-induced birefringence.

We have already made the assumption that the entry window of the GQC exhibits birefringence, and hence we may model it as a linear retarder of a retardence β_1 with arbitrary azimuth θ_1. The Jones Matrix for this situation

is given by Piazza *et al.* [3]

$$S_1(\beta_1, \theta_1) = cos\,\frac{\beta_1}{2}\,\mathbf{I} + sin\,\frac{\beta_1}{2}\,cos\,2\,\theta_1\,\mathbf{i} + sin\,\frac{\beta_1}{2}\,sin\,2\theta_1\,\mathbf{k}\ , \tag{2.1}$$

where $\mathbf{I}$ is the unit matrix and $\mathbf{i}$ and $\mathbf{k}$ are the Pauli matrices:

$$\mathbf{I} = \begin{bmatrix} 1 & 0 \\ 0 & 1 \end{bmatrix},\ \mathbf{i} = \begin{bmatrix} i & 0 \\ 0 & -i \end{bmatrix},\ \mathbf{k} = \begin{bmatrix} 0 & i \\ i & 0 \end{bmatrix}.$$

The exit window of the GQC may be described by an equation for S_2 similar to (2.1). A physical rotation of the GQC is required in order to bring the wires into a vertical plane and this rotation will give rise to an error γ in the azimuth. The procedure for this rotation is described in the following chapter and here it suffices to say that it is accurate enough that the error in γ does not exceed 0.5% . We can then represent the Jones matrix for the quadrupole cell by

$$J_q(\delta, \gamma) = cos\,\frac{\delta}{2}\,\mathbf{I} + sin\,\frac{\delta}{2}\,cos\,2\,\gamma\,\mathbf{i} + sin\,\frac{\delta}{2}\,sin\,2\gamma\,\mathbf{k}\ , \tag{2.2}$$

where δ is the retardance of the GQC, which we assume to be a linear retarder.

The $\frac{\lambda}{4}$-plate is ideally manufactured for a specific wavelength and has a re-

tardance of $\frac{\pi}{2}$ radians. However, commercially-available $\frac{\lambda}{4}$-plates have been found to differ from this by as much as a few degrees and they may also exhibit a temperature dependence which further affects their retardance, thus further deviating from the ideal. Precisely for these reasons it is complicated to allow for the retardance of a $\frac{\lambda}{4}$-plate. These setbacks may however be accounted for if we simply model the retardance of the $\frac{\lambda}{4}$-plate by $(\frac{\pi}{2} + \phi)$ radians. This additional term ϕ may be of either sign and need not necessarily be small.

The primary purpose of the $\frac{\lambda}{4}$-plate is to convert the elliptically-polarised light emerging from the GQC back to a linear state of polarisation. It serves this purpose sufficiently well regardless of whether the azimuth of its fast axis is at the $\pm \frac{\pi}{4}$ radian setting. The possibility of small deviations ϵ from either of these settings must be accounted for. These deviations may be deliberate or result from an inaccuracy in alignment. Experimental verification has shown that ϵ may be of either sign and repeated tests show that it never exceeds 1%. Imrie [1] presents the complete algebra for the Jones matrix for the $\frac{\lambda}{4}$-plate, and we need not discuss it here.

2.3 Consequences of the Jones calculus analysis

In previous induced-birefringence work [2], the quarter-wave plate has been offset by a small angle ϵ_1 and a plot of the PSD output (which is proportional to the intensity I/I_0) as a function of the induced rotations θ was made. Here, I_0 is the intensity of the beam leaving the polariser, and I is the intensity reaching the photodiode. Theoretically a zero PSD output will occur at $\theta_{null} = \frac{1}{2}\delta$, where δ is the phase difference. Pierrus [2] showed that because of strain birefringence in the cell windows, alignment errors in the GQC and analyser, and deviations from the ideal retardance of the quarter-wave plate, the intensity at θ_{null} is not zero. To remedy this Pierrus suggested an alternative procedure whereby θ_{null} may be found by plotting a second line that corresponds to a different $\frac{\lambda}{4}$-plate offset ϵ_2 on the same graph, the intersection of these graphs providing a θ_{null} value that has a small statistical error.

Imrie [1] showed that this method did not account for the effects of the deviations from ideal retardance of their $\frac{\lambda}{4}$-plate, resulting in measurements that were at least 5% too low or too high. He suggested an alternative method to remedy this problem, which entailed fixing the azimuth of the quarter-wave plate to either of the $\pm\frac{\pi}{4}$ settings and then plotting two lines corresponding

to oppositely-signed offsets α_1 and α_2 of the analyser. He obtained

$$\theta_{null} = -\frac{1}{2}\delta\left(\pm cos\,\phi - 2S_2 sin\,\phi\right) \tag{2.3}$$

where S_2 is the strain birefringence of the exit window. If ϕ is small then the $2S_2\,sin\,\phi$ term is at least two orders of magnitude smaller than the corresponding strain contribution $2S_2$, and we may ignore it [1]. Provided ϕ is small, we may approximate $cos\,\phi \approx 1$ so that $\theta_{int} = \mp\frac{1}{2}\delta$. Since our quarter-wave plate has a retardance of better than $90° \pm 0.5\%$, the error introduced by the approximation $cos\,\phi \approx 1$ is less than 0.01%. The technique developed by Imrie [1] is used in this work to determine the null current and hence ${}_mQ$. An example of the type of graph obtained using this technique is shown in Figure 2.2 below.

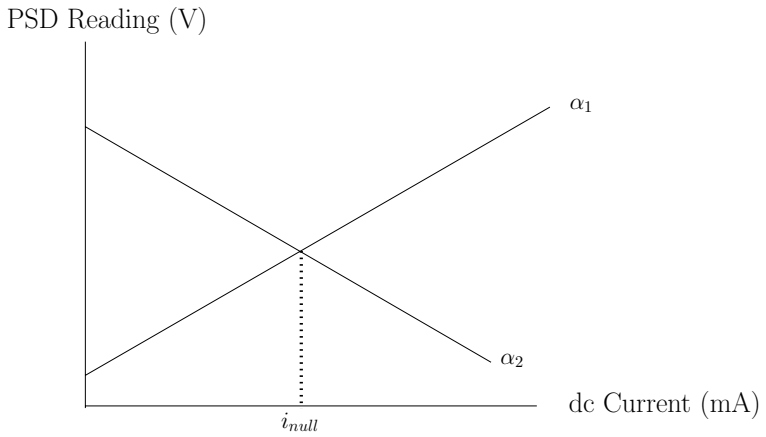

Figure 2.2: The graph of the analyser offsets and null current

2.4 The apparatus

The optics research group in Pietermaritzburg inherited most of the apparatus developed by Professor G. L. D. Ritchie's group [4, 5] in their experimental work. Watson describes this in great detail in his PhD thesis [5]. The only components of the original apparatus used in this work are the gas quadrupole cell (GQC) and the phase shifter, however these were modified to suit our experimental requirements. All of the other components were either custom built by the Electronics Center (EC) and/or Mechanical Instrument Workshop (MIW) at the University of KwaZulu-Natal (Pietermaritzburg), or purchased commercially. A detailed description of all the components used in this work is provided in the next chapter and we merely summarise the important apparatus here. A schematic of the apparatus used in this work is shown in Figure 2.3. In the figure the symbols P and Q denote the photodiode detector and quarter-wave plate respectively.

Modifications to the GQC and phase shifter

The GQC remained for the most part the same as its original manufacture save for a few minor modifications. Firstly the electrical feedthrough was modified so that operating voltages of up to 10 kV could be reached with little risk of corona discharges. The original macor ceramic cylinder was replaced with a teflon cylinder and the stainless-steel rod was sheathed by a teflon tube. Much disassembling and re-assembling of the GQC has oc-

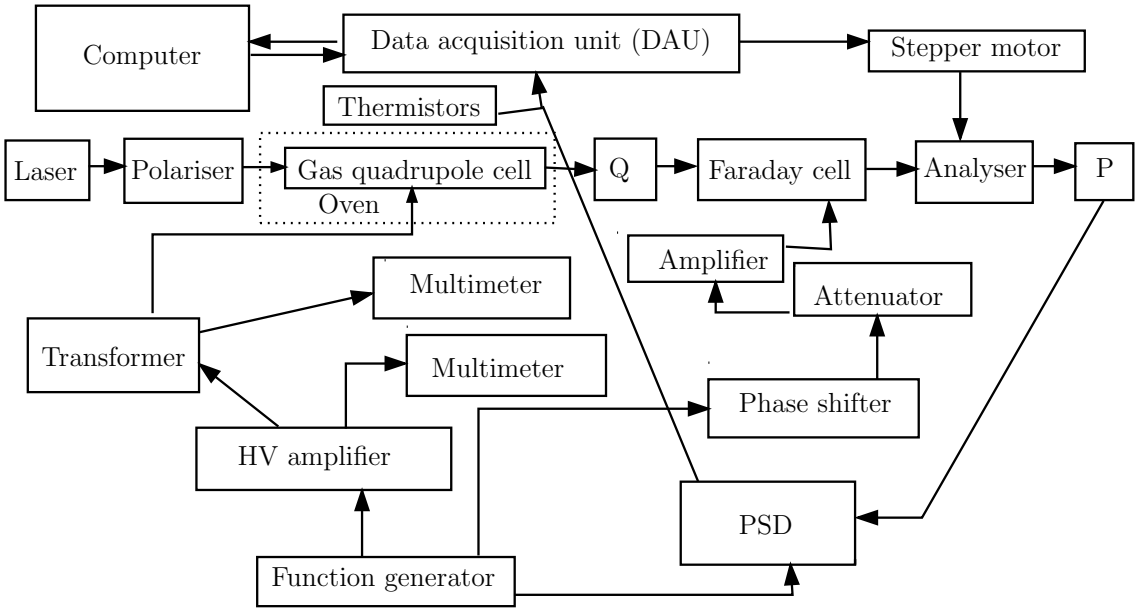

Figure 2.3: A schematic of the apparatus

curred throughout this work and the stainless-steel wires providing the field gradient have been changed on many occasions. No discernible deviation in experimental results was observed as a result of these changes.

Secondly the window mounts for the entry and exit windows were re-made to accommodate larger-diameter Pockels-glass windows and to allow for teflon seals to be used instead of viton. This was done so as to minimise the possibility of leaks developing at higher temperatures.

The phase-shifter control mechanism was also modified. A fine-control switch replaced the original coarse-adjustment switch on the front panel. This

switch allowed for very fine adjustments, to be made and thus enabled more control to be exercised when shifting the phase of the signal when setting up experimental runs.

Other apparatus

The Faraday cell (FC) used in this work differed from the conventional liquid-based cells typically used by other research groups in that it used as its rotating medium a solid piece of Pockels glass. It proved to be a very effective Faraday rotator and an important feature of this component was its stability. Numerous calibrations over the duration of this work have shown that the calibration constant of this cell differed by less than 0.4%.

The analysing prism mount was fitted with a stepper motor custom built at the MIW. An HP Basic program enabled the computer to communicate with the motor via the data-acquisition unit and hence allowed the prism to be rotated to the desired position. Very fine adjustments to within 0.07° to the rotation were possible with this system.

The ac function generator, multimeters, data-acquisition unit, oven-temperature controller, phase-sensitive detector (PSD), and the laser were all commercially purchased. The oven was specifically designed to fully enclose the GQC, and was constructed at the MIW. A major design requirement was the thermal insulation of the oven which was critical in protecting the sur-

rounding optical components, electronics, and computer from excessive heat at the higher temperatures. The oven-temperature controller used a PID algorithm to ensure that the set temperature of the oven was reached to within a degree.

The cumulative data reported in this thesis have taken more than two full years of observation time, recorded during both the day and the night. This has allowed for a reduction in the statistical uncertainties of the reported quadrupole moments and hyperpolarisabilities. This was made possible by automation of the observations through a computer-controlled IEEE interface linked to the apparatus. An HPBASIC program (listed in Appendix A) would instruct the computer to direct a sequence of measurements, as well as switch relays on and off to activate the stepper motor and hence rotate the analysing prism, etc. Once initiated, the experiment would run without human intervention, allowing for measurements to be taken throughout the night. This allowed for contributions to signal noise arising from building vibrations to be kept to a minimum.

The other apparatus which is shown in the schematic, but has not been discussed here, will be covered in the next chapter.

2.4.1 Experimental procedure

A brief outline of the experimental procedure is provided below.

1. An ac current was applied to the Faraday cell. This enabled the PSD to lock onto a reference signal.

2. The analyser and polariser were then crossed.

3. The analyser was then rotated to the α_1 setting, which is a small ($< 1°$) offset from null, as discussed below.

4. The current to the Faraday cell was then switched off and an ac high voltage (HV) was applied to the wires. This was typically in the region of 3 kV.

5. The phase of this signal was then set to zero on the PSD.

6. The HV to the wires was then switched off and an ac current was re-applied to the FC. The phase of the FC signal was monitored on the PSD, and the phase shifter was then used to shift the phase of this to be exactly 180° out of phase with the signal from the high voltage.

7. The HV to the wires was re-applied and the pressure reading was recorded.

8. The computer program was then executed and measurements commenced.

Once the analyser and polariser had been crossed, the stepper motor was used to rotate the analyser to a predefined offset position below the null point. This is the α_1 position, and light now reached the photodiode. The

current through the FC was then incrementally increased by the attenuator so that the signal would be between minimum and maximum readings on the PSD. A total of ten equally-spaced current values were recorded together with the corresponding PSD output, HV reading, and the temperature of the gas within the cell. The analyser was then rotated to the other predefined offset position α_2, which was above the null position, and another ten readings were made. A least-squares regression was then performed on the α_1 and α_2 data sets and a null current was determined from the intersection point of the two lines. Measurements of the null currents continued until the HP Basic program was stopped by human intervention.

A typical measurement period lasted for approximately three hours for carbon dioxide and nitrous oxide and up to six hours each for carbon monoxide, carbonyl sulphide and hydrogen. Overnight measurements lasting for not less than eight hours were also made. In order to obtain a reasonable statistical average with a low standard deviation, this process was repeated for approximately two weeks per temperature per gas. At the higher temperatures more averaging was required due to the smallness of the signal and the instability in the experiment, and thus measurement time sometimes extended to three to four weeks per temperature depending on the gas. For the gases studied in this project, we worked at five temperatures for carbon dioxide and six for nitrous oxide, carbon monoxide, and hydrogen in the temperature range of 22 °C to 200 °C. Measurements on carbonyl sulphide were performed at

room temperature only, the reason for which will be discussed in Chapter 4.

The null currents together with the corresponding pressure and temperature readings were then inputted into a Fortran90 computer program which then calculated the molar volume, electric field gradient, and molar Buckingham constant ${}_mQ$. For each gas, a graph of the ${}_mQ$ values against the inverse temperature was then plotted using the Microcal Origin graphical package. These graphs were in the form of straight lines, the slopes being used to deduce values for the electric quadrupole moments, while the intercepts provided values for the quadrupole hyperpolarisabilities.

2.5 The EFGIB experiment

In order to extract values of the electric quadrupole moment and the quadrupole hyperpolarisability of a particular molecule from (1.46), it is necessary to plot a graph of the Buckingham constant ${}_mQ$ as a function of inverse temperature. To accurately obtain ${}_mQ$, the birefringence $n_x - n_y$, molar volume V_m, electric field gradient E_{xx}, and temperature T must be determined.

The birefringence is not directly measured, instead the experiment is designed to measure the phase retardation induced in the light beam by the applied field gradient. The laser beam emerging from the gas quadrupole cell has an ellipticity characterised by δ, the retardance. The retardance is

related to the birefringence by

$$\delta = \frac{2\pi\, l}{\lambda}(n_x - n_x), \tag{2.4}$$

where λ is the wavelength of the laser beam and l is the path length in the medium.

The relatively small magnitude of the retardance (of the order 10^{-7} rad) gives rise to a large source of uncertainty. This quantity must thus be measured very accurately to minimise the uncertainty. One technique to achieve this is to use a calibrated compensater for measurement. Common compensaters are the Kerr nulling cell and the Faraday coil. After much consideration it was decided to use a Faraday coil with Pockels glass as the compensater in our experiment. This will be discussed further in the following chapter.

2.6 Possible sources of error

We recall that the equation defining ${}_mQ$ for a linear non-dipolar molecule, given in (1.46), is

$${}_mQ = \frac{2\,(3\epsilon_r + 2)\,N_A}{225\epsilon_r\epsilon_0}\left[\frac{15}{2}B + \frac{\Delta\alpha\,\Theta}{kT}\right]. \tag{2.5}$$

This equation contains three fundamental constants, and the values used for these were [6]:

- $\epsilon_0 = 8.85419 \times 10^{-12}\ \mathrm{C^2\,N^{-1}\,m^{-2}}$
- $k = 1.38065 \times 10^{-23}\ \mathrm{J\,K^{-1}}$
- $N_A = 6.02214 \times 10^{23}\ \mathrm{mol^{-1}}$

Equations (2.4) and (2.5) contain several experimental variables, the values of which need to be determined accurately. The wavelength λ of the laser beam is well known to be 632.8 nm [7], while the path length l through the medium was measured to be (1800 ± 0.5) mm. Linear expansion of the stainless-steel cell led to a fractional change in l of 0.25% over the full experimental temperature range utilised in this work, i.e. 22 °C to 200 °C.

The temperature T of the cell was calculated by averaging the readings of three PT100 platinum RTD's (Model 362-9840) that were evenly spaced over the length of the cell. These RTD's were calibrated directly from the factory and were found to be accurate to within 0.2 °C. The three individual readings when averaged provided a reading for the temperature inside the cell that was accurate to within 0.3%.

The molar volume V_m was calculated using the pressure virial coefficients provided over a large temperature range as tabulated by Dymond *et al.* [8]. This calculation relied on accurate readings of the gas pressures, and these were achieved using a Budenberg Master test gauge capable of reading pressures up to 4 MPa. The accuracy of this gauge was determined by calibrating

it against a Budenberg dead weight tester, and it was found to have a maximum error of 0.1%. Taking this error into account together with possible errors from the least-squares fit of the virial coefficient data, the maximum error in the calculation of the molar volume was estimated to be 0.3%.

The method for measuring the electric field gradient by considering the geometry of the cell is outlined by Buckingham and Disch [9]. To accurately calculate the electric field gradient requires that the position and size of image charges used to represent the wires and inner surface of the cell be known. Vrbancich [10] provides relationships that enable the above to be calculated:

$$\begin{aligned} q &= \frac{4\pi\epsilon_0 V}{ln\left(\frac{a^2}{2rd}\right)} \\ \lambda &= \frac{q}{2}\left[\frac{r^2\left(2d-b\right)}{d\left(2bd-b^2+r^2\right)}\right] \\ b &= \frac{r^2\left(4d^2-r^2\right)}{4d\left(2d^2+r^2\right)} \\ t' &= \frac{a^2}{d-b} \\ t &= \frac{a^2}{d} \end{aligned} \tag{2.6}$$

where

- q and λ are respectively the line of charge and image line of charge within the same boundary,
- V is the voltage applied to the wires,

- b is the distance between q and λ,
- $2d$ is the distance between the wires as measured from the centre of each of the wires,
- r is the radius of the wire, and
- a is the internal radius of the earthed quadrupole cell.

The electric field gradient may then be calculated from the above relations via [10]

$$E_{xx} = \frac{1}{\pi\epsilon_0}\left[\frac{q}{t^2} - \frac{q}{d^2} + \frac{\lambda}{(d-b)^2} - \frac{\lambda}{t'^{\,2}}\right]. \tag{2.7}$$

The wire spacing was measured at three points along the length of the cell and the average of these three values was used in calculating the electric field gradient. It was estimated that the maximum error in this reading was 0.3%. The applied high voltage was read directly by a precision Hewlett Packard (Model 3478A) multimeter. Periodic calibration of the high-voltage supply ensured the accuracy of its measurement. A maximum error of 0.1% was attached to this reading and hence we estimate that the overall error in the calculation of the electric field gradient was 0.4%.

Other possible sources of error will be discussed in the following chapters when they arise. The apparatus used in this experiment will be more comprehensively covered in Chapter Three.

Bibliography

[1] D. A. Imrie, *PhD Thesis, University of Natal (Pietermaritzburg)* (1993)

[2] J. Pierrus, *PhD Thesis, University of Natal (Pietermaritzburg)* (1989)

[3] R. Piazza, V. Degiorgio and T. Bellini, *Opt. Commun.,* **48**, 400 (1986)

[4] J. Vrbancich, M. P. Bogaard and G. L. D. Ritchie, *J. Phys. Sci. Instrum.,* **14**, 166 (1981)

[5] J. N. Watson, *PhD Thesis, University of New England* (1994)

[6] P. J. Mohr and B. N. Taylor, *Rev. Mod. Phys.,* **77**, 1 (2005)

[7] Melles Griot Laser Group, *Operation and Information Manual,* **ECM Technologies**, (1993)

[8] J. H. Dymond, K. N. Marsh, R. C. Wilhoit and K. C. Wong, *The virial coefficients of pure gases and mixtures,* **Springer**, (2002)

[9] A. D. Buckingham and R. L. Disch, *Proc. Roy. Soc. A,* **273**, 275 (1963)

[10] J. Vrbancich, *PhD Thesis, The University of Sydney (Sydney)* (1979)

Chapter 3

Apparatus

3.1 Introduction

The apparatus used in this project may be broadly divided into four divisions, namely

1. the support structures,
2. the optical train,
3. the supply structures, and
4. the detection system.

The features of the apparatus and equipment used in each of these divisions are now discussed in greater detail.

3.2 The support structures

3.2.1 The optical bench

The most important requirement of the optical bench is that it needs to be mechanically stable. It serves to isolate the components in the optical train from vibrations present in the surroundings, and hence minimise their contribution to signal noise.

The optical bench consists of a brick wall of height 96 cm upon which is cemented a granite slab of dimensions

- height 60 mm,
- width 910 mm, and
- length 3330 mm.

3.2.2 The optical rail

The optical rail consists of two H-section steel rails placed in parallel to each other. Each of these rails is supported by four adjustable feet which are used to level the rails. Rubber pads are placed under these feet to help damp out any external vibrations.

3.2.3 The optical stands

The optical stands have to provide a stable housing for both the optical components and the detector. They were manufactured from steel with their bases indented so as to fit snugly onto the H-section rail. To ensure that the components are stable and rigid, L-shaped clamps with wing nuts extend from either side of the stand bases to clamp a base plate onto the underside of the rail. Figure 3.1 below shows this clamping mechanism.

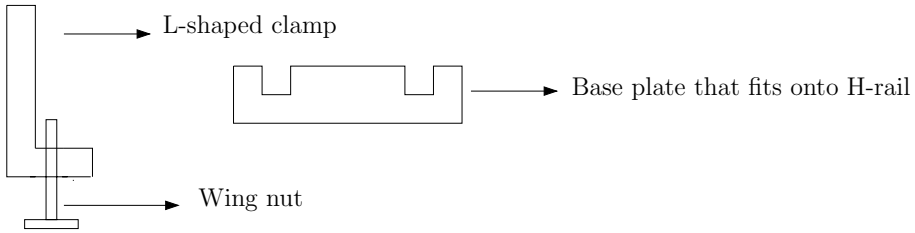

Figure 3.1: The clamping mechanism

Left and right adjustment screws on the base of each optical stand allow for fine adjustments in the horizontal direction. At the top of each stand is a locking screw which serves to lock a brass rod inserted into the base. Optical components are then attached to the top of each rod. These rods are 260 mm in length and are threaded over half their length. An adjustable threaded ring travels on this threaded region to provide vertical adjustment. This design thereby allowed for full adjustment (both horizontal and vertical) of the position of optical components. A schematic of the stands is shown in Figure 3.2 while the photograph in Figure 3.3 shows the stands in typical use.

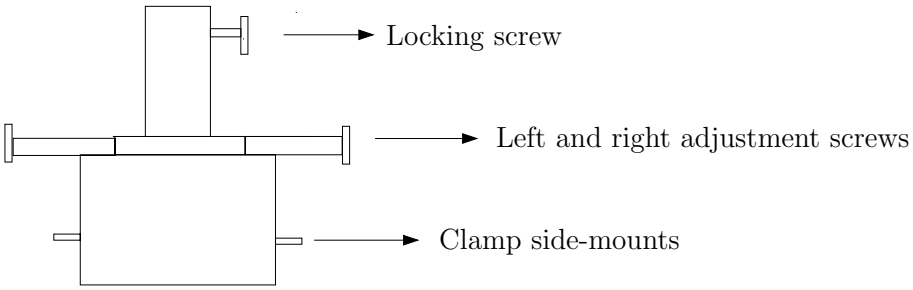

Figure 3.2: The stands

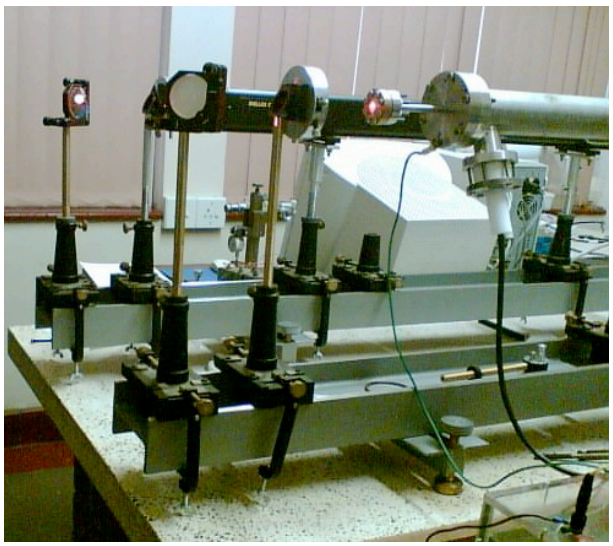

Figure 3.3: The stands with the optical components in place

3.3 The optical train

The optical components used in this work are shown schematically in Figure 3.4 below. They were mounted onto the optical rail using the stands described above. Each component in this train is described below.

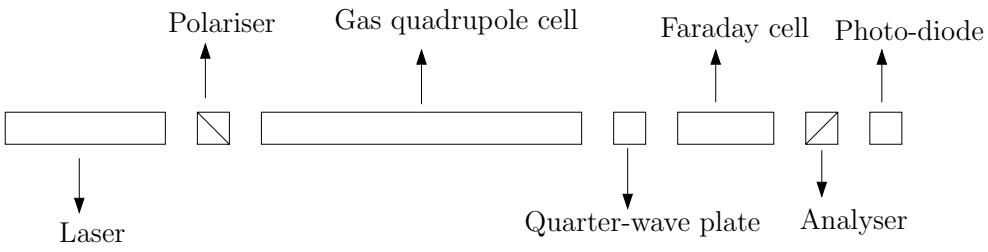

Figure 3.4: The optical train

3.3.1 The laser

A linearly-polarised Melles-Griot (Model 25 LHP 928-230) high-power HeNe laser was used in this work. It has a maximum power rating of 35 mW, yields a beam of wavelength 632.8 nm and it operates in the TEM_{00} mode with a beam diameter of 1.23 mm at the $\frac{1}{e^2}$ points. The manufacturer quoted a beam divergence of 0.66 mrad with the beam waist being located at the outside surface of the output mirror.

The laser could not be placed directly in front of the quadrupole cell as indicated in the optical train in Figure 3.4 due to the length of the cell, and in order to overcome this limitation two rails were placed in parallel, the laser being situated on one rail, its beam being steered to the second rail using two mirrors as shown in Figure 3.5. The losses from manipulating the light in this way are less than 2% and hence do not affect our measurements significantly. Any depolarisation that may occur through reflection is removed by passing the beam through a polariser on the main axis of the optical train.

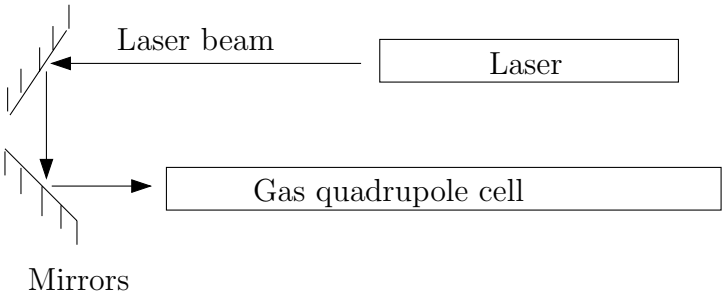

Figure 3.5: Laser beam steering

3.3.2 The prisms

The polariser and analyser are both Glan-Thompson prisms. They are manufactured by the Karl Lambrecht Corporation, and have 8 mm clear apertures. The prisms are mounted in precision rotators (Model 13011) manufactured by the Oriel Corporation. These precision rotary stages provided stable and highly accurate circular motion, free of wobble or play. A thumb screw provided for coarse 360 degrees manual rotation. Fine adjustments were possible with the use of a micrometer drive. The angle of rotation can be measured by reading the 360 degree scale followed by the vernier scale, which is read in millimetres and is converted to an angular rotation in degrees via the conversion $1^0 \equiv 0.635$ mm. This rotator provides a high-resolution setting to within 0.1 arc seconds, which is ideal for this investigation. A photograph of the precision rotator is shown in Figure 3.6 below.

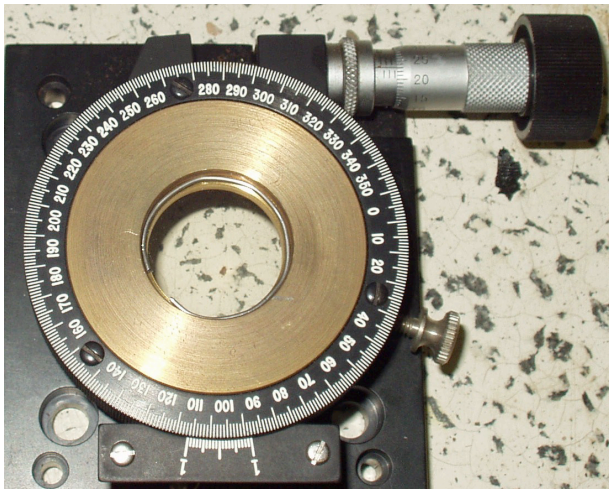

Figure 3.6: The precision rotator used for mounting the prisms

3.3.3 The quarter-wave plate

A Newport model 05RP04 zero-order quartz quarter-wave plate, specifically manufactured for use with a source of wavelength $\lambda = 632.8$ nm, was used in this investigation. The quarter-wave plate was mounted in a precision rotator similar to the one described above, and has a retardance better than $90° \pm 0.5\%$.

3.4 The supply structures

3.4.1 Introduction

The gas quadrupole cell (GQC), designed and manufactured by Professor Ritchie's research group [1, 2] in Armidale, has three main requirements; namely that it should

1. withstand a pressure range from vacuum to $\approx$ 3500 kPa,

2. withstand a temperature range from room temperature to 230 °C, and

3. withstand application of a high potential of up to 10 kV to the parallel wires without discharging.

The gas quadrupole cell constructed by the Armidale group meets all of these design requirements, and is now discussed in detail.

3.4.2 The gas quadrupole cell

The cell is constructed from a tube of 1818 stainless steel, and has a length of 2010 mm, an inner diameter of 54.6 mm, and a wall thickness of 3.0 mm. The window housings are mounted on stainless-steel tubes which are supported by stainless-steel end-caps, and are attached to the cell by means of stainless-steel flanges that are bolted to each end of the cell with stainless-steel bolts.

The cell is typically operated at gas pressures of 2.5 MPa, and needs to be leak free so as to maintain the pressure for the duration of the experimental process. A possible source of leaks is the the region were the end caps are attached to the cell. Viton O-rings were used as a seal between the flanges and the end-caps and were found to eradicate any leaks from this region.

The windows are housed in brass cylinders. These cylinders were manufactured by the Mechanical Instrument Workshop from solid brass rounds that had been turned and hollowed out at the centre so as to accommodate the windows. Windows are sandwiched between teflon O-rings in this cavity. This again provides an excellent leak-free seal. Schott SF 57 glass of diameter 25.0 mm and thickness 5.0 mm is used for the cell windows. The window housings were mounted on stainless-steel tubes that extended 70.0 mm from the cell so as to render any retardation induced in the glass by the applied electric-field-gradient negligible.

To allow the wire spacing to be measured, the cell has three pairs of viewing ports along its length. These ports are similar to those of the window housings described above. The windows used for the viewing ports are made from fused silica and are mounted at the end of 50.0 mm lengths of stainless-steel tube, which are then welded into holes bored along the length of the cell. Double welds on either side of the cell wall ensure that these joints are leak free. A schematic of the cell is shown in Figure 3.7 and the corresponding photograph in Figure 3.8 below.

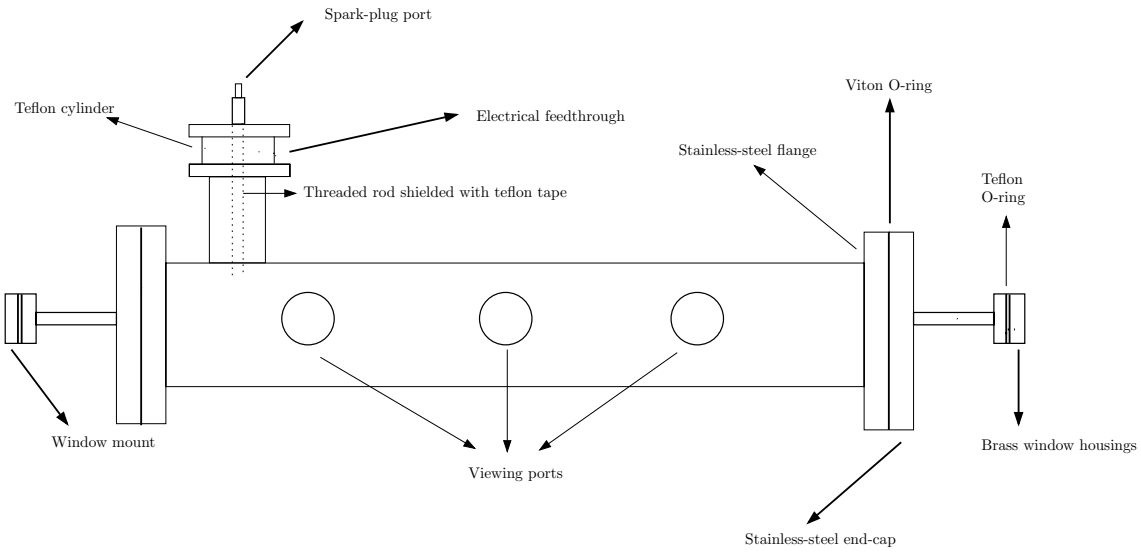

Figure 3.7: A schematic of the gas quadrupole cell (not to scale)

Figure 3.8: A photograph of the gas quadrupole cell

The pair of wires that is at a high voltage and hence induces an electric field gradient [3] between them is held fixed in place by two wire holders that are located on the inside of the cell. In addition these wire holders also provide the required tension in the wires. Two small tensioning mechanisms, shown in Figure 3.9 below, are located at one end of the cell to allow the required tension in the wires to be set using a torque wrench.

Figure 3.9: The tensioning mechanism

A stainless-steel spring-loaded device is located on the opposite end of the tube, and is used to maintain the tension in the wires. This is shown in Figure 3.10 below.

A stainless-steel plate is located at the front of each of the wire holders. Three holes are precisely drilled into this plate to ensure that the wires are separated at a fixed distance from the cell wall and from each other. This

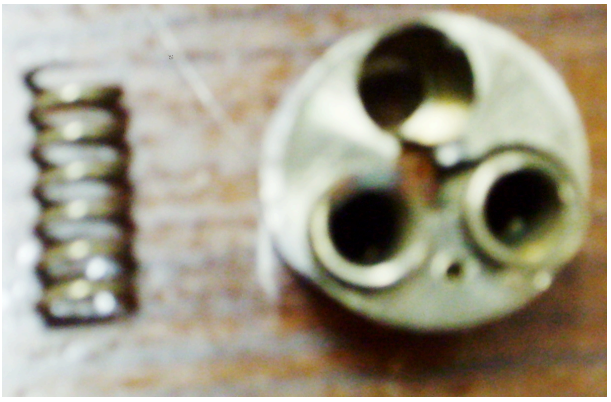

Figure 3.10: The spring-loaded device

also facilitates alignment of the laser beam, ensuring that it passes between the wires. The free flow of gas through the cell, when it is being filled or evacuated, has been allowed for by drilling more holes into the plate. This is shown in the Figure 3.11 below.

Figure 3.11: The stainless-steel plate showing the three holes

The insulating rings that locate the wire holders within the outer sleeve of

the gas cell have to be made of a carefully selected material that will remain serviceable under the stresses imposed in the experiment. Macor ceramic glass was chosen for the mountings since

1. the glass has a maximum operating temperature of 1300 K,
2. at high voltages the glass is an excellent insulator,
3. it is resistant to most chemicals, and
4. it is mechanically very stable.

A schematic of the wire-tensioning mechanism is shown in Figure 3.12 below.

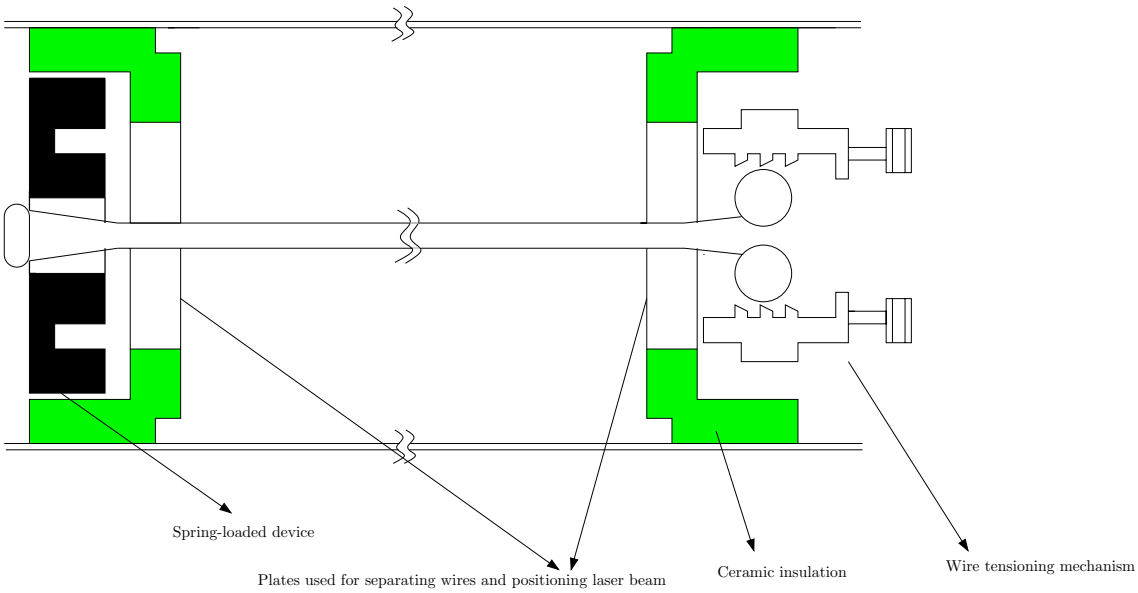

Figure 3.12: The quadrupole cell interior

Electrical feedthrough to the GQC

The electrical feedthrough is provided by a stainless-steel rod, sheathed by a teflon tube that runs through the centre of a teflon cylinder. This rod is threaded at both ends. The connection to the wire-holder is effected by means of a small length of stainless-steel wire that is attached to the end of the feedthrough. The wire has been enclosed by teflon tape to minimise corona points, which can lead to discharge of the high voltage. This arrangement is shown in Figure 3.7 above. Corona discharges at the high operating voltages are not only a serious physical hazard to the experimentalist, but they are also a source of radiation and hence noise that could potentially degrade the performance of the apparatus. Extensive tests were performed to ensure that the risk of corona discharge was minimised.

Vertical alignment of the wires

It is absolutely essential that the two wires parallel to the axis of the horizontal GQC lie in a vertical plane. Misalignment will affect not only determinations of the wire spacing, but also calculations of both the phase difference δ and the electric field gradient E_{xx}. In order to achieve precise alignment, we employed two techniques. The first method was used when the cell wires were replaced or re-tensioned. Initially the wires were placed into their holders and partially tightened. Before maximising the tension in the wires, a cathetometer was used to check if the wire holders had been inserted vertically.

The cross-hairs of the cathetometer were set to the vertical using a commercial Bosch PCL 1 laser level that produced an extremely accurate cross-beam as a reference. Any misalignment in the wire holders was thus easily detected and corrected by manually rotating the holders until the desired position was reached. They were then clamped in place and the wires were tensioned to the maximum desired tension. Many tests were conducted and the optimal tension for the wires was found to correspond to a torque-wrench setting of 60 N cm when tightening the tensioning mechanism.

The second method we used was only employed once the cell had been reassembled and replaced in the optical train. Laser light was allowed to pass through the cell and a diffraction pattern, clearly showing the wires, was produced. A magnified pattern was obtained by using a lens to project the diffraction pattern onto a screen. True vertical was again determined by using the laser level as a reference.

Any misalignment of the wires from vertical was thus detected, and corrected by gently rotating the entire GQC until true vertical was reached. The cell would then be clamped in place. This method of alignment guaranteed that the error in the vertical setting was limited to less than 0.5%.

3.4.3 The power supplies

Introduction

The high alternating voltage applied to the cell wires is generated by a unique system designed by our EC incorporating a signal source, amplifier, and a dual transformer which steps up the voltage in one transformer, and stabilises it through feedback with a signal from the second step-down transformer. A sinusoidal ac signal, set at a frequency of 363 Hz, is generated by a GE (Model GFG-8015G) signal generator and provides the reference signal in this experiment. A commercial amplifier could have been used, however we chose to have one built to a specified stability of $< 0.1\%$, thus providing a very stable voltage to the wires and in turn achieving a very consistent electric field gradient.

The uniqueness of this system is the dual transformer arrangement [4] which is now discussed.

The high-voltage supply

The basic circuit diagram of the amplifier is shown in Figure 3.13 and a photograph of the amplifier appears in Figure 3.14.

The signal from the function generator, which needs to be set to between 120 and 180 mV, passes through a transconductance amplifier. It then passes to

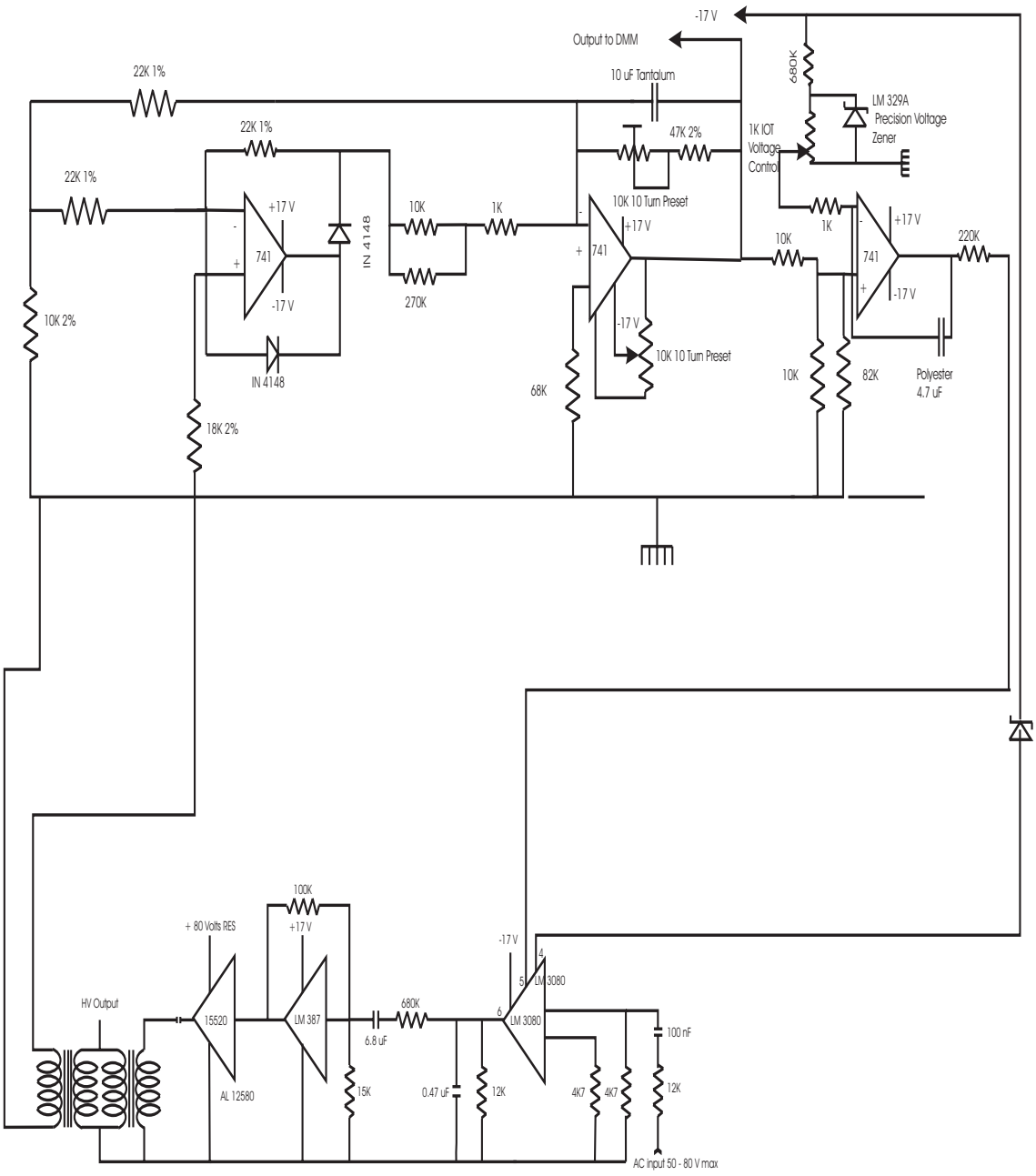

Figure 3.13: The amplifier circuit diagram

Figure 3.14: The amplifier and monitoring apparatus

a preamplifier which feeds the power amplifier that drives the output transformer. The output transformer is the first of the two transformers, and it has a step-up turns ratio of 1000:1.

The second transformer is a 1:1000 step-down transformer connected to the HV source output. This transformer is used to monitor the output voltage on a digital meter and serves to keep the output voltage constant through feedback. Since typical working voltages are of the order of 3 kV, it is necessary to ensure that there is no risk of arcing between the transformers. Placing the transformers into a perspex container filled with transformer oil, as shown in Figure 3.15, achieves this requirement.

The stepped-down voltage from the monitoring supply is applied to a precision operational-amplifier full-wave rectifier. High precision (0.1% and better), low-temperature potentiometers are used to obtain stable and highly-

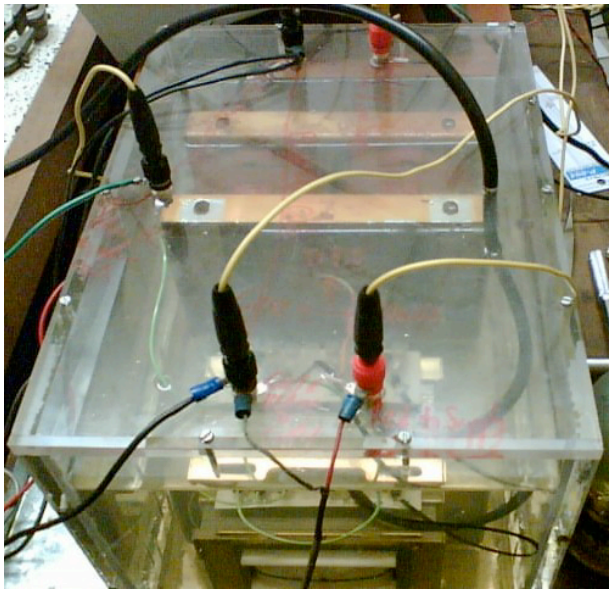

Figure 3.15: The dual transformers soaked in a bath of transformer oil

accurate dc output. This dc signal is adjusted by a scale factor, so that the true rms voltage applied to the cell can be read directly off a multimeter. As a result of this scaling, a one volt dc reading on the digital meter corresponds to a 1000 volt rms voltage applied to the wires of the cell. The accuracy of this scaling was periodically checked by measuring the voltage applied to the cell wires by means of a HV probe, and checking the corresponding reading on the digital meter. A graph of these two values was plotted over a suitable range and the slope was checked for agreement between the scaled reading and the actual rms voltage on the wires. The agreement was found to be better than 0.4% over the 1 to 10 kV range.

3.4.4 The gas line

The gas line is an essential part of the supply structures since the high purity of the gas needs to be maintained when transferring the gas from the storage cylinder into the GQC. Our gas line is shown in Figure 3.16 below.

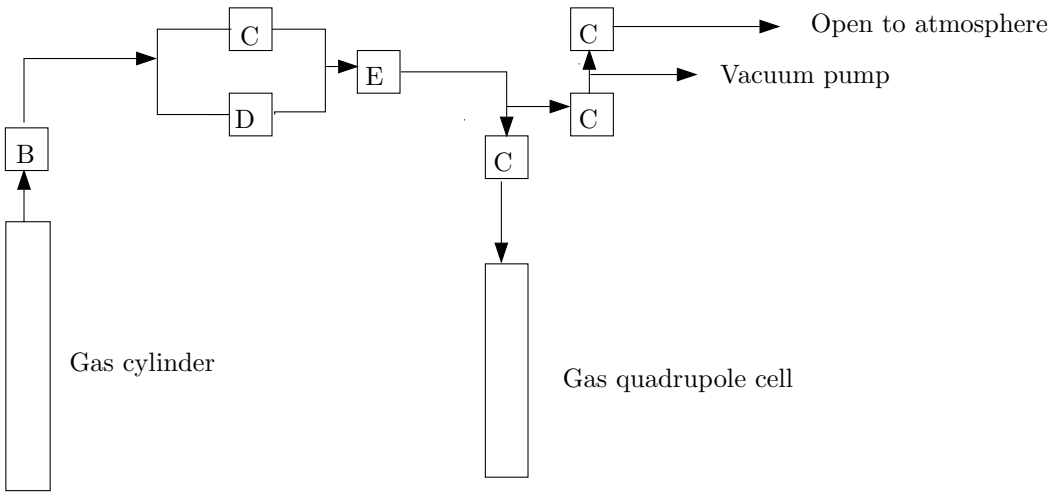

Figure 3.16: The gas line

In the diagram the labels have the following association:

- B represents the regulator,
- C is a Hoke coarse-metering valve,
- D is a Hoke fine-metering valve, and
- E is a 0.2 μm millipore filter

All of the gas samples used in this work were of the highest purity that could be commercially obtained. The gas cylinders were regulated to safe working pressures, and supplied either a fine-metering valve or a coarse-metering valve placed before the 0.2 μm filter. The fine-metering valve is used when the cell is being filled so as to prevent the millipore filter from tearing. The coarse-metering valve is used when the line needs to be evacuated.

The 0.2 μm millipore filter serves to remove any dust particles that may be present in the gas from the cylinder and it is followed by another coarse-metering valve used to isolate the gas cell from the gas line once it has been filled.

Another coarse-metering valve is used to isolate the GQC and the gas line from the vacuum pump. A final coarse-metering valve is used to open the vacuum-pump line to the atmosphere. This valve is opened when the vacuum pump is to be switched off so as to prevent suck back of the vacuum-pump oil into both the gas line and the GQC. The joins in the line are all stainless-steel Hoke fittings and the line itself is stainless-steel pipe of 3 mm inner diameter. A braided flexible hose is used to link the gas line to the gas cylinder. For safety reasons all gas cylinders are secured to a bracket on the wall using steel chains.

The gas samples were allowed to flow very slowly into the cell, it generally

taking approximately two hours for the cell to be filled to 2.5 MPa. Once filled the GQC was allowed to equilibrate for a sufficient period of time, generally around eight hours, to ensure that the cell windows stabilised from the induced strain resulting from the filling of the cell.

3.4.5 The Pockels-glass Faraday cell

Most Faraday rotators used in our electro-optical experiments have been toluene based, however toluene is a toxic fluid and it is volatile and hence evaporates easily. This evaporation of toluene from the cell means that the level of toluene in the Faraday rotator needs to be monitored so as to ensure it is at the correct level at all times. This is tedious and if neglected would lead to unreliable results.

With this in mind it was decided to construct a Pockels-glass Faraday rotator. Pockels glass has a very low residual strain birefringence which makes it an ideal rotator. We obtained, as a generous gift from Professor G. L. D. Ritchie, a rod of Pockels glass of dimensions 11.93 cm in length and 1.40 cm in diameter. The Pockels glass is shown in Figure 3.17 below. This glass melt was commissioned by Professor A. D. Buckingham and it is unique in that it was slowly cooled so as to minimise residual stresses in the glass. MIW was asked to construct a solenoid, the cylinder of Pockels glass lying coaxial with the solenoid air core so that the glass could be tested for its effectiveness as a Faraday rotator. The coils consisted of 7140 turns of a thin gauge (0.5 mm)

Figure 3.17: The Pockels glass used in the Faraday rotator

copper wire and 100 turns of a thicker (1.2 mm) gauge copper wire. The solenoid had a length of 136.75 mm and an internal diameter of 34.05 mm. Figure 3.18 shows the completed rotator.

The effectiveness of this Pockels-glass Faraday rotator was determined as follows.

Faraday-cell calibration

Our aim was to determine the solenoid current required to induce a particular rotation in the plane of polarisation of linearly-polarised laser light passing through the Faraday cell. The cell was calibrated by applying a dc voltage across the 100 turn coil: this is the coil that needs to be calibrated since it is used to null the birefringence signals in the EFGIB experiment. A small ac current is simultaneously applied through the 7140 turn coil. A 492.5 mH inductor was included in series with the 100-turn coil to prevent coupling between the coils. The ac signal was provided by a GE (Model GFG-8015G)

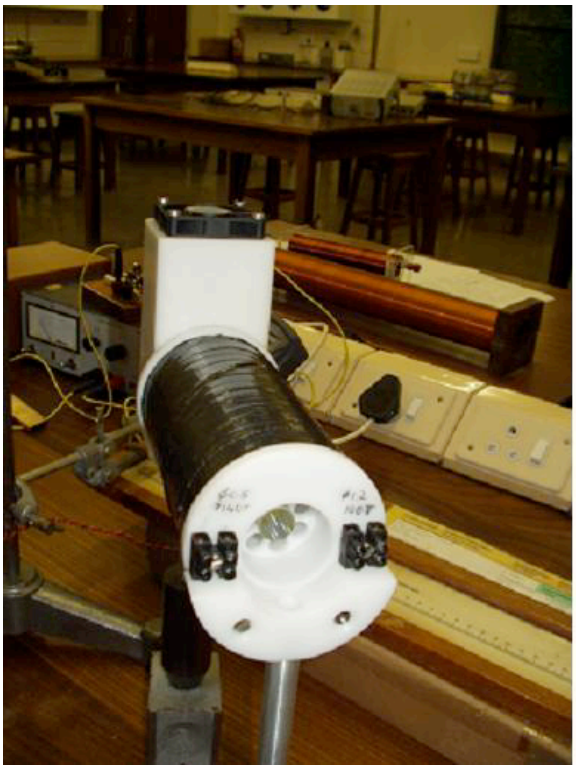

Figure 3.18: The Faraday rotator

waveform synthesizer, this being fed into an amplifier so as to amplify the current through the coil. This current leads to an alternating magnetic field which serves to modulate the light. The phase sensitive detector (PSD) can then lock onto this modulated signal as measured by the photodiode detector. The optical train used in the calibration of the Faraday cell is illustrated in the block diagram in Figure 3.19 below, while the electronic components are depicted in the block diagram in Figure 3.20, also shown below. A photograph of the apparatus is shown in Figure 3.21.

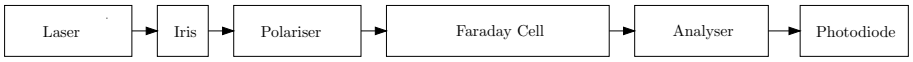

Figure 3.19: Block diagram of the optical train

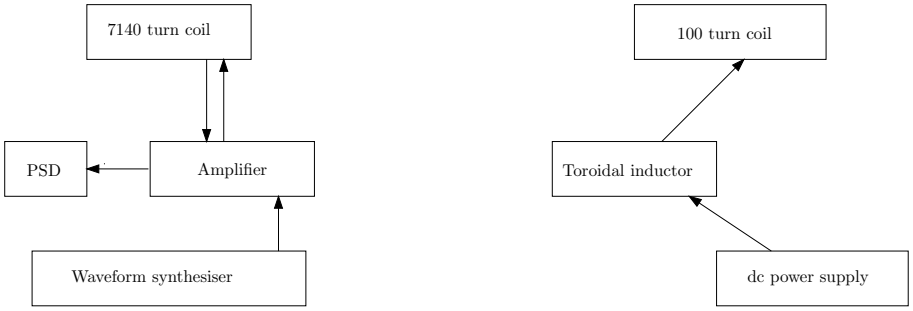

Figure 3.20: Block diagram of the electronic components

A micrometer was connected to the analyser rotation stage to allow for small known rotations. This micrometer was adjusted until the output on the PSD read zero (i.e. to regain a null signal, the analyser and polariser being crossed). The micrometer reading was then recorded for that particular current. To complete the calibration (and hence to be able to obtain fairly accurate rotations by knowing the current required to induce a particular rotation) we proceeded to record measurements of the current and the corresponding micrometer readings required for null over a wide range of current values.

Figure 3.21: The apparatus used in the calibration of the Faraday cell

Results

As a dc current was passed through the 100 turn coil, the light emerging from the Faraday cell was manually nulled by rotating the analyser prism. The various dc currents passed through the 100 turn coil, together with the micrometer reading corresponding to each null, are recorded in Table 3.1 below.

The best-fit straight line through the points is shown in Figure 3.22. A linear regression revealed a correlation coefficient of 0.9996 with a slope of $(7.06 \pm 0.07) \times 10^{-5}$ in mA^{-1}. This is converted to rad mA^{-1}, yielding the

Table 3.1: dc currents and the corresponding micrometer reading at null

dc Current (mA)	Micrometer reading (inches)
11.10	0.2700
106.30	0.2768
214.10	0.2853
299.30	0.2906
401.10	0.2970
504.10	0.3048
606.48	0.3124
708.50	0.3180
810.50	0.3260
912.00	0.3348
1047.50	0.3436

calibration constant θ for the Faraday cell to be

$$\theta = s \times 0.0243879 \tag{3.1}$$

where θ is the rotation of the prism in radians and s is the distance the micrometer moves in inches. The slope of the graph then becomes $(173 \pm 2) \times 10^{-8}$ rad/mA.

Conclusion

We found that the Pockels glass worked extremely well as a Faraday rotator, and can be used as a retarder in electro-optical experiments with confidence. Its calibration constant has been accurately determined, allowing known rotations to be induced by applying the required current through the 100 turn coil. This proved extremely useful when nulling optical signals in the EFGIB experiment.

The supply to the Faraday cell

When nulling electric-field-gradient-induced birefringences, an ac current needs to be passed through the coil of the Faraday rotator in order to induce nulling rotations in the plane of polarisation of the light beam emerging from the GQC. The sinusoidal ac signal originates from the same signal generator supplying the high-voltage controller. This signal is fed into a phase shifter which sets the phase of the ac current entering the Faraday cell. Current in

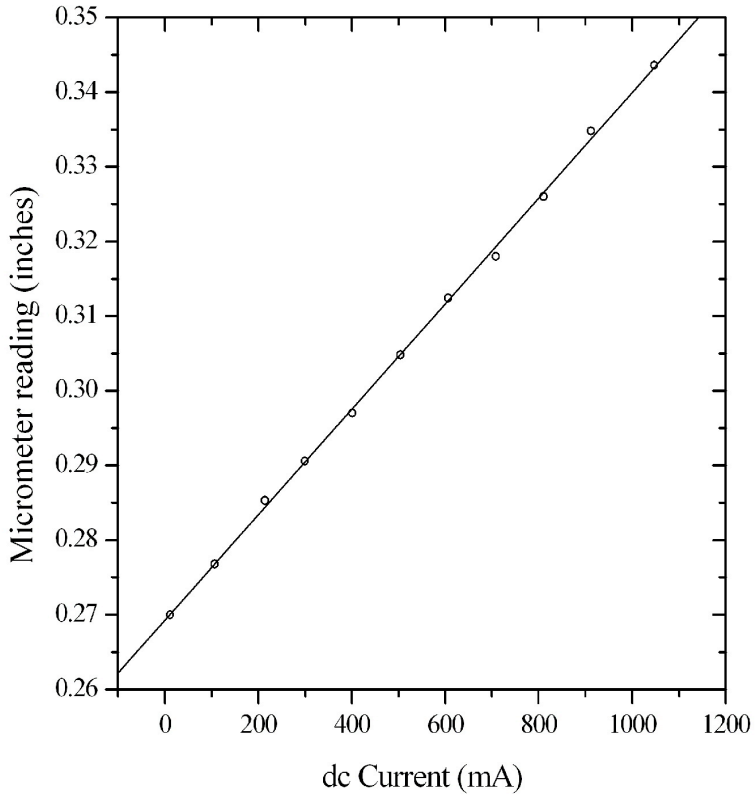

Figure 3.22: Plot of micrometer readings (inches) vs current (mA) to determine the calibration constant of the Pockels-glass Faraday rotator cell

the Faraday cell needs to be set exactly in anti-phase to the signal emerging from the GQC.

Once appropriately phase shifted the signal is then fed into an attenuator. This attenuator has been designed by the EC and it is described in detail below. The signal from the attenuator is then sent to an amplifier which am-

plifies the signal so that correct current is passed through the Faraday coil to produce the required rotations. Figure 3.23 below shows a photograph of this system.

The ac attenuator

In order to obtain a set of ac current readings which range from full-scale readings (positive and negative) on the PSD, the sense or phase of the ac current passing through the Faraday rotator must be able to be phase shifted through 180°, and this is achieved by the attenuator. A computer is used to control the attenuator via the data acquisition unit (DAU) relays. The computer and DAU will be discussed in Section 3.5. A count mechanism of 0-512 steps is built into the attenuator. The first half of the count (0-256) supplies 0-200 mV while the second half of the count (257-512) supplies the same voltage but in anti-phase. An HP Basic computer program was written to divide the count range into ten equally-spaced voltages, ranging from the minimum to the maximum PSD full-scale readings.

The attenuated voltage is then applied to the Faraday coil via the amplifier using a second set of DAU relays. A third set of DAU relays is used to set the attenuator to zero after each run. The EC-built attenuator is a modified version of the DAC0832 [5], 8-Bit μP compatible, double-buffered D to A converter. The modifications made entail using the DAC (Digital to Analog Converter) for ac current inputs and outputs instead of the intended

design specification of dc current. The DAC0832 is an advanced CMOS 8-Bit multiplying DAC designed to interface directly with a microprocessor. A deposited silicon-chromium R-2R resistor-ladder network divides the reference current.

The circuit uses CMOS current switches and control logic to achieve low power consumption and low-output leakage-current errors. Special circuitry provides TTL logic input-voltage compatibility. This system was chosen for the following reasons, and it proved to be ideal for use in this experiment:

- Current settling time: $1\mu s$
- Resolution: 9-Bits
- Linearity: 8, 9 or 10 bits (guaranteed over temperature)
- Low power dissipation: 20 mW

An explanation of the terms used above follows:

- Resolution: Resolution refers to the number of switches within the DAC. For example the DAC0832 has 2^9 or 512 steps and therefore has 9-bit resolution.
- Settling time refers to the amount of time it takes from a code transition until the DAC output reaches $\pm \frac{1}{2}\%$ of the final output value.

The various electronic components discussed above are depicted in the photograph in Figure 3.23.

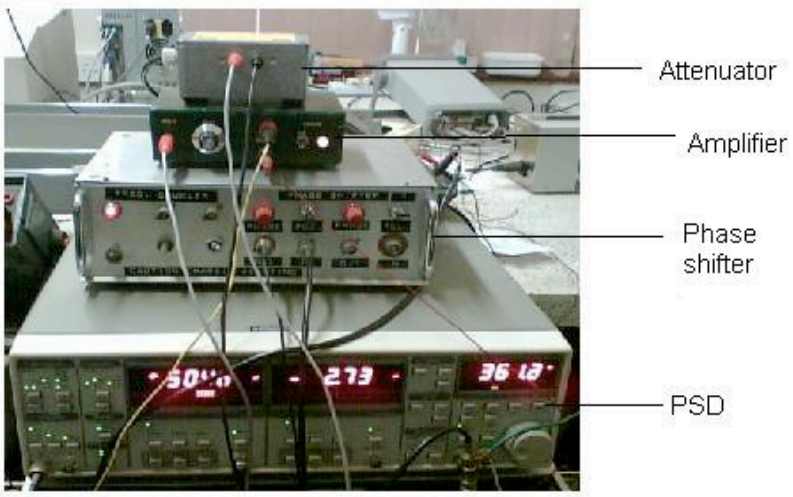

Figure 3.23: The supply electronics

3.4.6 The stepper motor

In order to determine the null current in the present EFGIB work, use was made of the technique developed by Graham *et al.* [7] and refined by Imrie [8]. In order to proceed with experimental measurement the analyser must be rotated to a small ($< 1°$) offset either side of null, namely α_1 or α_2. This is easily achieved by manually rotating the precision-rotator housing of the analyser. When computer controlled, manual rotations (though possible) are not convenient. It is with this in mind that a stepper motor has been fitted to the analyser micrometer and this enables the rotations to be automated.

The stepper motor is controlled by the computer via the data acquisition unit, both of which are described in Section 3.5.

Each stepped rotation of the stepper motor corresponds to a 0.010 mm rotation on the micrometer. This can in turn be converted to a rotation of the prism in degrees, as explained in Section 3.3.2.

The stepper motor is mounted onto a threaded brass rod that fits into a base similar to the optical stands described in Section 3.2.3. This stand allows for alignment of the motor in the horizontal direction while the threaded brass rod allows for movement in the vertical direction. These adjustments allow the motor to be positioned parallel to the analyser to prevent cogging. A hexagonal channel and a hexagonal shaft mechanism fixes the motor to the analyser micrometer, allowing the micrometer to slide along the hexagonal shaft as it travels in and out.

The stepper-motor stand is mounted onto an I-rail that is in turn rawl bolted to the optical bench. There is a layer of padding between the base and the I-rail as well as between the I-rail and the optical bench, which helps to minimise transference of the vibrations arising during motor rotation to the optical bench and its components. The stepper motor and its mounting are shown in Figures 3.24 and 3.25 below.

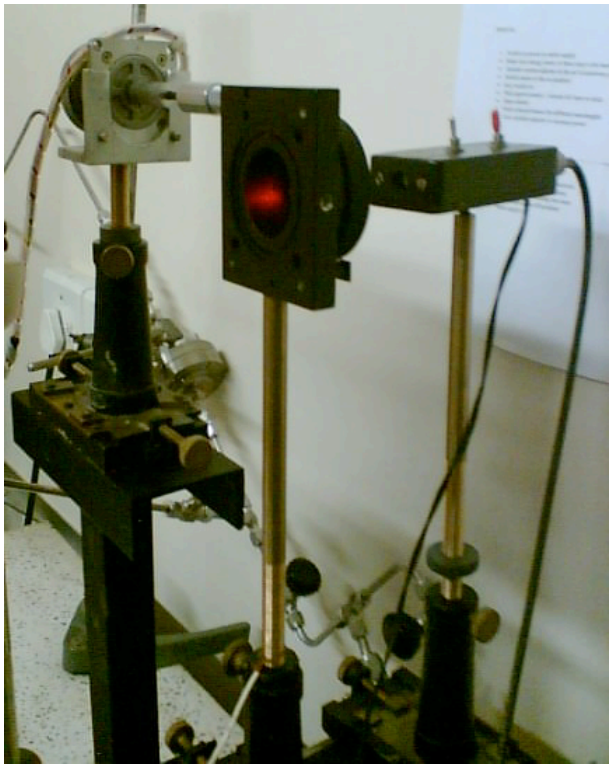

Figure 3.24: The stepper motor and its mounting

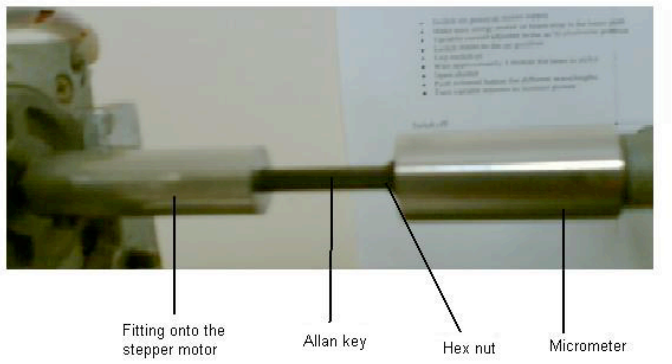

Figure 3.25: The stepper motor linked to the micrometer

3.4.7 The oven

In order to perform a study of the temperature dependence of the effect it is necessary to heat the GQC. The MIW and EC assisted in the design and construction of an air oven that surrounded the GQC, and the main requirements of this oven were that

- it be able to reach temperatures of up to 250 °C,
- it provide heat evenly over the length of the cell, eliminating hot and cold spots,
- it not heat the electronic and optical components close to the cell, and
- it be able to heat quickly and maintain the set temperature to within $\pm 1°C$.

The oven which was designed met all of the requirements listed above. A piece of sheet metal 2.20 m long, 1.10 m wide, and 5 mm thick was formed into a U-shape to form the base of the oven. A second sheet of metal of the same thickness was formed into a second U-shape that fitted into the base surrounded by a 5 cm gap. This space was filled with Fibreflax, an insulation material capable of withstanding temperatures of up to a thousand degrees celcius. Calculations showed that a 5 cm layer this material would be adequate in minimising heat losses through the oven walls. A front view of the oven is shown in Figure 3.26 below. The base of the oven was supported by two stands at either end that allowed the height, as well as horizontal

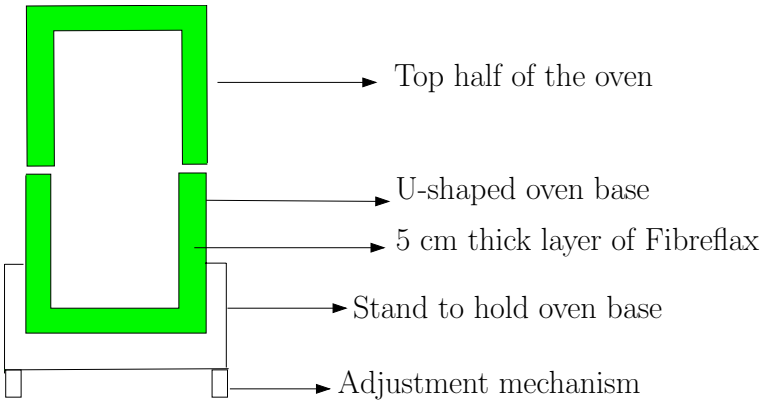

Figure 3.26: Front view of the oven

position, to be adjusted. Two holes were drilled to allow the stands holding the GQC to fit through. This setup allowed the GQC to sit directly in the centre of the oven. Very fine positioning adjustments were made possible by this arrangement, which also made adjustment of the GQC possible without having to open the oven. This was especially useful at elevated temperatures. Another hole 6 mm in diameter was drilled through the oven wall to allow the thermistors to be fed through to the cell. To complete the oven, a top half was manufactured with the same specifications as the base, the only differences being that the top half was designed to allow for the high voltage feedthrough and it was not directly supported by stands, but rather rested on the base itself. A schematic of the oven is shown in Figure 3.27 below.

The top half of the oven was secured in place by three opposing sets of heavy duty canopy clips that were evenly spaced along the length of the oven, locking the oven in place. Two sheet-metal end caps, with 20 mm

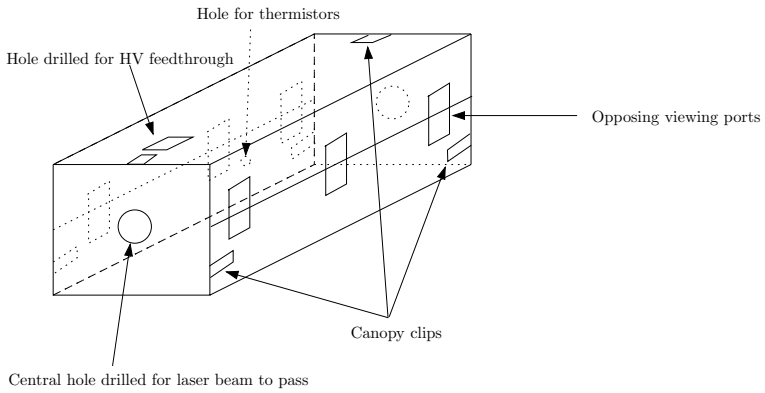

Figure 3.27: Schematic of the oven

holes drilled through the centre to allow the laser beam to pass through, were manufactured. They were lined with a 5 cm thick layer of Fibreflax. Strategically placed canopy clips secured these end caps to both the base and top half of the oven. An aluminium pipe of 2 mm wall thickness and 15 mm inner diameter was attached to the end windows of the cell and extended through the central hole in the end caps. This was done so as to allow the laser beam to pass into the cell unaffected by any turbulence inside the oven.

After setting up the oven it was found that heat loss at the oven joints was substantial at high temperatures. To remedy this, sheets of solid Insulite board were placed along the length of the oven to good effect. This material was chosen since it had properties similar to the Fibreflax but was a solid board so that it could be used without having to redesign the oven.

Heating of the oven was achieved by two parallel 2.5 kW heater elements,

each of length 2 m, fixed to the base of the oven. Included in the base were two recessed fans which could be used to circulate the air inside the oven in the case of uneven heating.

To ensure that the elements heated to the set point temperature, a commercial PID control device was purchased and modified by the EC to suit our requirements. The controller was chosen for two main reasons:

1. it had an in-built safety mechanism that switched off the elements in the case of any mechanical failure, potential discharges or power failures. This was particularly useful in the case of overnight runs when the operator was not present to monitor and rectify any problems that arose. Also it prevented fire hazards and damage to equipment or the oven itself in the case of the elements switching on to full power when restarting after a power failure.

2. the controller had the required PID algorithm and consequent stability to ensure that the elements could be controlled such that the oven set point could be maintained to within ± 1°C.

The temperature inside the cell was monitored by three PT100 (Model 362-9840) platinum resistors that were spaced out along the length of the cell. These resistors showed the temperature inside the cell to vary by no more than 0.2 °C along its length, substantiating the evenness and stability of the heating mechanism. The average reading of these three resistors provided

the recorded temperature of the gas inside the cell. A top view of the cell inside the oven base is shown in Figure 3.28 below. The picture clearly shows the pockets which house the thermistors, as well as the recessed fans.

Figure 3.28: Top view of the cell inside the oven base

3.5 The detection system

3.5.1 The light detector

The light passing through the analyser is incident on a photodiode detector. This silicon detector has a diameter of 6 mm, and the electronics for the detector were built by the EC. The signal from the photodiode detector is sent via a shielded co-axial cable to the phase-sensitive detector.

3.5.2 The phase-sensitive detector

A Stanford Research Systems (Model SR830) lock-in amplifier was used in this work. Some of its features are [9]

- a full scale sensitivity of 2 nV to 1 V,
- a reference channel frequency range of 1 mHz to 102 kHz,
- a phase resolution of 0.01°,
- a time constant of 10 μs to 30 s for reference frequencies above 200 Hz and up to 30 000 s for reference frequencies below 200 Hz, and
- a 4 $\frac{1}{2}$ digit LED display for channel 1, channel 2 and the reference channel.

In this work the PSD was set to a sensitivity of 200 μV and was placed on a one second time constant.

3.5.3 The multimeters

The multimeters were used primarily as monitoring tools rather than actual measuring instruments since all measurements were taken by the data acquisition unit and sent to the recording PC via a GPIB interface. Nonetheless the multimeters played an important role in ensuring that the correct voltages were applied to the cell when manually setting up runs, as well as allowing for quick checks of the stabililty of the supplies during a run.

A Hewlett Packard (Model 3478A) multimeter was used to monitor the high voltage supplied to the cell. A second HP multimeter (Model 3478A) was used to monitor the ac current passing through the Faraday cell.

A Fluke (Model 45) dual-display multimeter was used to periodically check the output frequency of the function generator, the supply voltage to the high-voltage amplifier, as well as the output of the high-voltage amplifier. This meter was chosen for this purpose since it had a dual display that allowed two properties of an input signal (eg. frequency and ac voltage) to be displayed at the same time [10]. It also had a compare mode which allowed the user to determine whether a measurement was within, above or below a designated range. This meter proved very efficient in performing the measurements listed above.

3.5.4 The data-acquisition system

The experiment is fully automated by computer control, and this was achieved through the use of an Agilent (Model 34970A) data acquisition/switch unit (DAU). This section describes the data-acquisition system currently in use.

The Computer

A Pentium 3 computer is used to communicate with the DAU. This personal computer has 256 Mb of RAM and an 80 gigabyte hard drive with a CPU operational frequency of 1700 MHz. The computer runs an HP Basic program (listed in Appendix A) to control the DAU.

The data acquisition unit

An Agilent (Model 34970A) DAU is used in this work. The features of this unit are [11]:

- $6\frac{1}{2}$-digit multimeter accuracy, stability and noise rejection,
- up to 60 channels per instrument,
- reading rates of up to 600 readings per second on a single channel and scan rates of up to 250 channels per second,
- standard GPIB (IEEE-488) interface, and
- standard commands for programmable instruments (SCPI) compatibility.

The DAU formed the heart of the computer control with an HP Basic program using the DAU's multimeter function to measure the high voltage applied to the cell, the ac current through the Faraday cell, as well as the temperature in the room (via a J-type thermocouple) and the temperature inside the cell (via PT100 resistors).

The DAU was also used to control the stepper motor via the use of its relays, as well as to control the current attenuator, again with the use of relays. This DAU proved to be highly reliable and robust and ensured ease of measurement, often running continuously for several days.

A Fortran90 computer code (listed in Appendix B) was written to analyse the data collected by the DAU, allowing for calculation of the molecular electric quadrupole moment for the molecule under investigation. The code for all the molecules studied in this work is essentially the same, with the only significant changes being to the virial coefficient values, dielectric constants, and polarisability anisotropies.

Bibliography

[1] J. Vrbancich, M. P. Bogaard, and G. L. D. Ritchie, *J. Phys. Sci. Instrum.,* **14**, 166 (1981)

[2] J. N. Watson, *PhD Thesis, University of New England* (1994)

[3] A. D. Buckingham, *J. Chem. Phys.,* **30**, 1580 (1959)

[4] I. C. D. Stuckenberg, *PhD Thesis, University of Natal (Pietermaritzburg)* (1984)

[5] National semiconductor product manual, *www.national.com, accessed 05 December 2005*

[6] J. Pierrus, *PhD Thesis, University of Natal (Pietermaritzburg)* (1989)

[7] C. Graham, J. Pierrus, and R. E. Raab, *Molec. Phys.,* **67**, 9939 (1989)

[8] D. A. Imrie, *PhD Thesis, University of Natal (Pietermaritzburg)* (1993)

[9] Stanford Research Systems Product Manual, *Model SR830 DSP Lock-In Amplifier* (2001)

[10] Fluke and Philips Product Manual, *Model 45 Dual Display Multimeter* (1989)

[11] Agilent Product Manual, *Model 34970A Data Acquisition / Switch Unit* (2003)

Chapter 4

Results and discussion

4.1 Carbon dioxide (CO_2)

4.1.1 Introduction

Several independent measurements of the molecular electric quadrupole moment of carbon dioxide have been obtained by means of the electric-field-gradient-induced birefringence (EFGIB) technique over the past 45 years [1-6]. The quadrupole moment has also been measured by a range of other methods [7-11], and its value is now well-established [5], providing an ideal benchmark against which to assess the performance of our apparatus.

This work was performed using Coleman-grade high-purity carbon dioxide (CO_2). The gas was supplied by Air Products and has a stated minimum purity of 99.99%. Second and third pressure virial coefficients were required

when calculating the molar volumes of the gas samples. These were extracted from the tabulations provided by Dymond *et. al* [12].

Buckingham [13] has shown that the effective optical electric field and the applied field gradient are enhanced by the polarisation of the surroundings of a molecule. The effective field gradient is $\frac{2\epsilon_r+3}{5}$ times larger than the applied field gradient. This correction can account for as much as 1.5% of the value of the electric quadrupole moment, which is far from negligible, and hence this factor has been included in (1.45) and has been used in all results reported in this Chapter.

We can obtain a value for the dielectric constant ϵ_r by making use of the Clausius-Mosotti function expanded in terms of inverse molar volume:

$$\left(\frac{\epsilon_r - 1}{\epsilon_r + 2}\right) V_m = A_\epsilon + \frac{B_\epsilon}{V_m} + \frac{C_\epsilon}{V_m^2} + \cdots \tag{4.1}$$

where

- ϵ_r is the static dielectric constant,
- A_ϵ is the first dielectric virial coefficient,
- B_ϵ is the second dielectric virial coefficient, and
- V_m is the molar volume.

For carbon dioxide ϵ_r was calculated using the values for the dielectric virial coefficients measured by Bose and Cole [8]. The optical-frequency polarisability anisotropy has been accounted for by using the value of $(2.350 \pm 0.071) \times 10^{-40}$ $\mathrm{C^2\,m^2\,J^{-1}}$ as measured at 632.8 nm by Bogaard *et al.* [14].

4.1.2 Results

A number of runs was performed on carbon dioxide at each of the desired temperatures ranging from room temperature up to *ca.* 200 °C. At the start of each run, the computer would instruct the stepper motor to rotate the analyser to its α_1 offset position. The cell temperature and high voltage signal would then be measured and recorded. The current through the Faraday cell coil would then be set to one of ten equally-spaced values, and after waiting for the PSD output to stabilise, 20 readings of the PSD voltage would be recorded and averaged. This process would be iterated for each of the desired Faraday cell currents, after which the program would perform a least-squares regression of the data, yielding a slope and intercept for the best-fit line. If the correlation coefficient was worse than 0.999, the line would be rejected and the measurement process repeated. Otherwise the analyser would be rotated to its α_2 offset, and the process iterated. The intersection point of the α_1 and α_2 lines yields the null current as discussed in section 2.6 of Chapter 2.

The final ${}_mQ$ results at each (averaged) experimental temperature are shown

in Table 4.1. The measurements were performed over a range of pressure, and with an average high voltage of *ca.* 3 kV applied to the wires. The room temperature varied between 22 to 29 °C. In all of the following analysis, the errors presented are the statistical errors associated with the measured quantities, and the systematic errors mentioned in Chapter 2 are not considered. A weighted least-squares regression analysis of ${}_mQ$ versus T^{-1} is performed to obtain the best-fit slope and intercept.

Table 4.1: The Buckingham constant ($_mQ$) values for carbon dioxide measured over a range of temperature and at 632.8 nm

$\overline{T}$ (K)	$P^\dagger$ (MPa)	$10^4 V_m{}^\dagger$ ($m^3\,mol^{-1}$)	$\varepsilon_r{}^\dagger$	$V^\dagger$ (kV)	$10^{-8} E_{xx}{}^\dagger$ ($V\,m^{-2}$)	$10^{26}\,{}_mQ^\ddagger$ ($C\,m^5\,J^{-1}\,mol^{-1}$)
299.4	2.635	8.087	1.029	3.054	-8.025	-25.42 ± 0.37
336.7	1.985	13.10	1.017	3.013	-10.62	-22.83 ± 0.48
366.3	1.840	15.77	1.014	3.046	-7.867	-20.81 ± 0.37
398.4	1.640	19.53	1.011	3.049	-7.626	-19.46 ± 0.42
471.7	1.120	34.96	1.006	3.078	-7.487	-16.36 ± 0.45

† These values are for a typical run and not the average values for all the runs performed since the pressure and the applied voltage varied between runs.

‡ This value is the average of all the runs (typically around 1000 null currents) obtained at a particular temperature.

4.1.3 Discussion

A plot of the tabulated Buckingham-constant values versus inverse temperature is shown in Figure 4.1 below, together with the weighted least-squares straight-line fit. The slope and intercept of the weighted fit are summarised in Table 4.2, which also includes the polarizability anisotropy, and the deduced quadrupole moment and hyperpolarisability term.

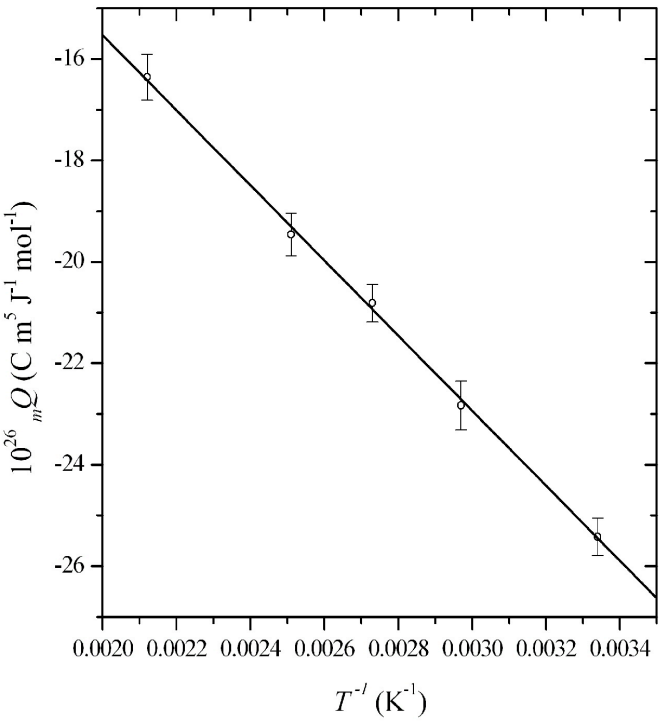

Figure 4.1: The temperature dependence of ${}_{m}Q$ for carbon dioxide

Table 4.2: Slope and intercept values extracted from the ${}_mQ$ vs T^{-1} graph, literature polarizability anisotropy required for the analysis, together with the quadrupole moment and quadrupole hyperpolarisability of carbon dioxide determined via equation (2.5)

Property	Value
10^{26} intercept ($\mathrm{C\,m^5\,J^{-1}\,mol^{-1}}$)	-0.74 ± 0.34
10^{23} slope ($\mathrm{C\,m^5\,K\,J^{-1}\,mol^{-1}}$)	-7.40 ± 0.14
10^{40} $\Delta\alpha$ ($\mathrm{C^2\,m^2\,J^{-1}}$)[14]	2.350 ± 0.071
10^{40} Θ ($\mathrm{C\,m^2}$)	-14.39 ± 0.71
10^{60} B ($\mathrm{C^3\,m^4\,J^{-2}}$)	-0.29 ± 0.13

Equation (2.5) allows for the quadrupole moment and the quadrupole hyperpolarisability to be deduced from the slope and intercept, respectively. We have

$$Slope = \frac{\Delta\alpha\,\Theta}{k}\left(\frac{2\,(3\epsilon_r+2)\,N_A}{225\epsilon_r\epsilon_0}\right) \Rightarrow \Theta = Slope \times \left(\frac{225\epsilon_r\epsilon_0 k}{2\,(3\epsilon_r+2)\,\Delta\alpha N_A}\right), \tag{4.2}$$

$$Intercept = \frac{15}{2}\left(\frac{2\,(3\epsilon_r+2)\,N_A}{225\epsilon_r\epsilon_0}\right) B \Rightarrow B = Intercept \times \left(\frac{550\epsilon_r\epsilon_0}{30\,(3\epsilon_r+2)\,N_A}\right). \tag{4.3}$$

The electric quadrupole moment of Θ = (-14.39 $\pm$ 0.71) $\times 10^{-40}$ $\mathrm{C\,m^2}$ obtained in this work compares almost identically with the experimental result of (-14.3 $\pm$ 0.6) $\times 10^{-40}$ $\mathrm{C\,m^2}$ obtained by Watson *et al.* [5]. Since Watson *et al.* [5] assumed that the effective field gradient was the same as the applied field gradient, setting $\epsilon_r = 1$ in the factor $\frac{2\epsilon_r+3}{5}$, we have recalculated our

Θ setting $\epsilon_r = 1$, which yields Θ = (-14.34 $\pm$ 0.71) $\times 10^{-40}$ C m^2, bringing the value even closer to that of Watson *et al.* This serves to confirm the reliability of our apparatus, and hence we can proceed to study other gases with confidence. It also highlights the need to use the effective field gradient, since setting $\epsilon_r = 1$ reduces the quadrupole moment measured here by 0.4%.

A quadrupole hyperpolarisability of B =(-0.29 $\pm$ 0.13) $\times 10^{-60}$ C^3 m^4 J^{-2} has been extracted from our measurements. It is interesting to note that setting $\epsilon_r = 1$ increases B by some 7% to B =(-0.27 $\pm$ 0.13) $\times 10^{-60}$ C^3 m^4 J^{-2}, which matches exactly with that of (-0.27 $\pm$ 0.13) $\times 10^{-60}$ C^3 m^4 J^{-2} obtained by Watson *et al.* [5]. Our B also compares favourably with the value of (-0.2 $\pm$ 0.3) $\times 10^{-60}$ C^3 m^4 J^{-2} obtained by Battaglia *et al.* [3]. This serves to confirm the small but non-negligible contribution of this term to the measured molecular quadrupole moment, the hyperpolarisability contributing some (2.7 $\pm$ 1.1)% to ${}_mQ$ at a temperature of 299.4 K. The most recent *ab initio* computation, at the MP2 level of theory, yields B = -0.39 $\times 10^{-60}$ C^3 m^4 J^{-2} [18], which lies within one standard deviation of our result.

Graham *et al.* [6] extracted a quadrupole moment from room-temperature EFGIB measurements by neglecting altogether the hyperpolarisability contribution, obtaining (-14.53 $\pm$ 0.22) $\times 10^{-40}$ C m^2. Re-analysing their data using our value for B, we obtain a quadrupole moment of (-14.14 $\pm$ 0.49) $\times 10^{-40}$ C m^2, which is within one standard deviation of our result. A tabulation

of our quadrupole moment for carbon dioxide, together with selected values obtained by other researchers, follows in Table 4.3; with a similar tabulated comparison for the quadrupole hyperpolarisability in Table 4.4.

Table 4.3: A comparison of selected molecular quadrupole moments for CO_2

$10^{40}\Theta$ ($C\,m^2$)	Method	Reference
-14.39 ± 0.71	EFGIB (temp. dependent)	this work
-14.3 ± 0.6	EFGIB (temp. dependent)	[5]
-14.98 ± 0.5	EFGIB (temp. dependent)	[3]
-14.53 ± 0.22	EFGIB (single temp., $B = 0$)	[6]
$-14.14 \pm 0.49^{\dagger}$	EFGIB (single temp., corrected for B)	[6]
$-14.3 \pm 0.8^{\ddagger}$	EFGIB (single temp., $B = 0$)	[1, 5]
-14.0 ± 0.8	magnetic anisotropy	[15]
-14.4	dielectric & pressure virial coefficients	[8]
-14.3 ± 1.3	collision-induced far IR absorption	[9]
-14.3	BD(T) computation	[16]
-14.29 ± 0.09	CCSD(T) computation	[17]
-14.3	CCSD(T) computation	[18]

†value in [6] corrected using our B =(-0.29 $\pm$ 0.13) $\times 10^{-60}$ $C^3\,m^4\,J^{-2}$
‡value in [1] rederived in [5] using updated molecular polarisability data

Before attempting measurements of any new molecule, trial carbon dioxide measurements would be performed and compared against the definitive value obtained here. If the measurements were found to vary by more than one

Table 4.4: A comparison of quadrupole hyperpolarisabilities for CO_2

$10^{60}B$ ($C^3\,m^4\,J^{-2}$)	Method	Reference
-0.29 ± 0.13	EFGIB (temp. dependent)	this work
-0.27 ± 0.13	EFGIB (temp. dependent)	[5]
-0.2 ± 0.3	EFGIB (temp. dependent)	[3]
-0.093	CCSD(T) computation	[17]
-0.39	MP2 computation	[18]

standard deviation from our result, a search would be made for the cause effecting this variation (e.g. slight misalignment in the optical train, a drift in the calibration of the high-voltage supply, etc.). Once found, the fault would be corrected, and more carbon dioxide trial runs would be performed before proceeding with measurements of the new molecule. Use of carbon dioxide as a standard reference also proved useful whenever the cell was dismantled and reassembled, or when operated at elevated temperatures.

4.2 Nitrous oxide (N_2O)

4.2.1 Introduction

Our literature search indicates that only two previous EFGIB measurements of the molecular quadrupole moment of nitrous oxide have been attempted, both at room temperature. A recent *ab initio* coupled-cluster investigation of this molecule [19] has yielded state-of-the-art calculated values of the quadrupole moment and quadrupole hyperpolarisability. The authors argue for a temperature-dependent EFGIB experimental investigation to be undertaken, so that a definitive comparison of experiment and theory can be provided for. With this in mind, it was decided to undertake a temperature-dependent study of nitrous oxide, and work was performed on an ultra-high-purity (UHP) sample with a quoted minimum purity of 99.999%, supplied by Air Liquide. N_2O is a polar molecule, and the term $A_{||} + 2A_{\perp} + \frac{10}{\omega}G'$ in equation (1.51) is zero, since the origin of the quadrupole moment has been defined relative to the effective quadrupole centre.

We have accounted for the effects of the dielectric constant ϵ_r, again making use of the Clausius-Mosotti function in equation (4.1). Kirouac and Bose [20] provide values for the first and second dielectric virial coefficients, while the dynamic polarisability anisotropy value of $(3.267 \pm 0.098) \times 10^{-40}$ C^2 m^2 J^{-1} for 632.8 nm is from the work of Bogaard *et al.* [14].

4.2.2 Results

As for carbon dioxide, a number of runs were performed at each temperature. Experimental results for nitrous oxide are given in Table 4.5 below.

Table 4.5: The Buckingham constant ($_mQ$) values for nitrous oxide measured over a range of temperature and at 632.8 nm

$\overline{T}$ (K)	$P^\dagger$ (MPa)	$10^4 V_m{}^\dagger$ ($m^3\,mol^{-1}$)	$\varepsilon_r{}^\dagger$	$V^\dagger$ (kV)	$10^{-8} E_{xx}{}^\dagger$ ($V\,m^{-2}$)	$10^{26}\,{}_mQ^\ddagger$ ($C\,m^5\,J^{-1}\,mol^{-1}$)
298.5	2.085	10.60	1.022	3.064	-7.849	-28.40 ± 0.42
325.7	1.465	17.38	1.013	3.044	-7.849	-25.99 ± 0.45
363.6	1.425	20.70	1.011	3.098	-7.028	-23.34 ± 0.61
393.7	1.323	22.23	1.010	3.057	-6.899	-21.71 ± 0.54
436.7	1.054	33.67	1.007	3.047	-7.505	-19.73 ± 0.65
473.9	1.118	34.73	1.006	3.021	-7.971	-18.36 ± 0.63

† These values are for a typical run.

‡ This value is the average of all the runs (typically around 1000 null currents) obtained at a particular temperature.

4.2.3 Discussion

A plot of the above Buckingham-constant values versus inverse temperature is shown in Figure 4.2 below, together with the best-fit straight line with error as weight. The slope and intercept of the weighted fit are summarised in Table 4.6, together with the extracted quadrupole moment and hyperpolarisability.

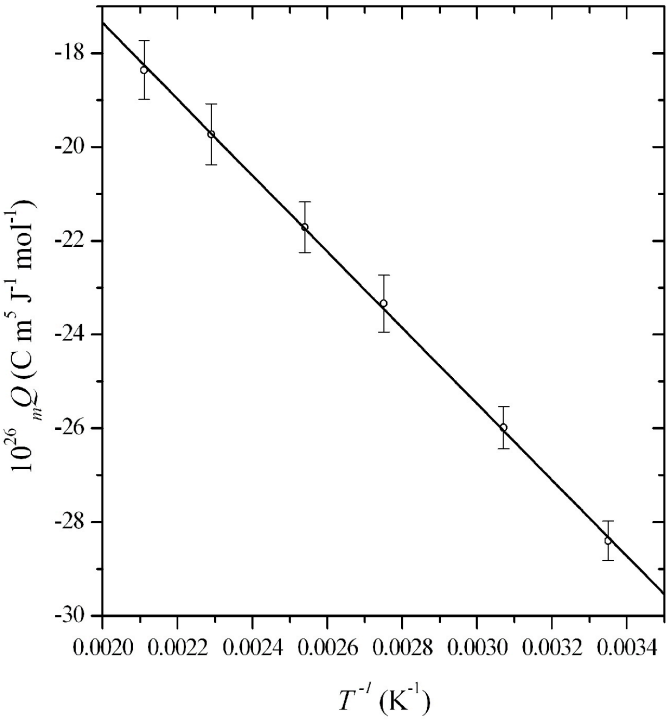

Figure 4.2: The temperature dependence of ${}_{m}Q$ for nitrous oxide

Table 4.6: Slope and intercept values extracted from the ${}_mQ$ vs T^{-1} graph, literature polarizability anisotropy required for the analysis, together with the quadrupole moment and quadrupole hyperpolarisability of nitrous oxide determined via equation (2.5)

Property	Value
10^{26} intercept ($\mathrm{C\,m^5\,J^{-1}\,mol^{-1}}$)	-1.12 ± 0.24
10^{23} slope ($\mathrm{C\,m^5\,K\,J^{-1}\,mol^{-1}}$)	-8.121 ± 0.086
10^{40} $\Delta\alpha$ ($\mathrm{C^2\,m^2\,J^{-1}}$) [13]	3.267 ± 0.098
10^{40} Θ ($\mathrm{C\,m^2}$)	-11.36 ± 0.46
10^{60} B ($\mathrm{C^3\,m^4\,J^{-2}}$)	-0.50 ± 0.11

At first sight, the quadrupole moment of $\Theta = (\text{-}11.36 \pm 0.46) \times 10^{-40}$ C m^2 for nitrous oxide obtained in this investigation appears to be in excellent agreement with that of $(\text{-}11.22 \pm 0.61) \times 10^{-40}$ C m^2 obtained by Buckingham *et al.* [21]. However, Buckingham *et al.* have assumed the contribution from the quadrupole hyperpolarisability to be negligible. We have obtained a value of $B = (\text{-}0.50 \pm 0.11) \times 10^{-60}$ C^3 m^4 J^{-2} from our measurements, and are now in a position to examine the extent to which the B term contributes to ${}_mQ$. We find that, at a temperature of 298.5 K, B contributes $(4.1 \pm 0.8)\%$ to ${}_mQ$, which is certainly too large to ignore. A re-analysis of the Buckingham *et al.* result [21] to account for the hyperpolarisability term's contribution yields a revised quadrupole moment of $\Theta = (\text{-}10.76 \pm 0.71) \times 10^{-40}$ C m^2, which now differs from our result by some 5.3%. The earlier result of Buckinghham *et*

al. [2] of (-11.7 ± 1.0) × 10^{-40} C m^2, when reanalysed using the more-recent polarisability anisotropy of (3.267 ± 0.098) × 10^{-40} C^2 m^2 J^{-1} [14], as well as taking into account our B-term value, yields Θ = (-11.4 ± 1.1) × 10^{-40} C m^2. This is in excellent agreement with our quadrupole moment. A comparison of our quadrupole moment for nitrous oxide together with selected values obtained by other researchers is contained in Table 4.7. The CCSD(T) computed quadrupole hyperpolarisability [19] is B = (-0.066 ± 0.09) × 10^{-60} C^3 m^4 J^{-2}, which is some 7.5 times smaller than our measured value.

Table 4.7: A comparison of selected molecular quadrupole moments for N_2O

$10^{40}\Theta$ (C m^2)	Method	Reference
−11.36 ± 0.46	EFGIB (temp. dependent)	this work
−11.22 ± 0.61	EFGIB (single temp., $B = 0$)	[21]
−10.76 ± 0.71†	EFGIB (single temp., corrected for B)	[21]
−11.7 ± 1.0	EFGIB (single temp., $B = 0$)	[2]
−11.4 ± 1.1‡	EFGIB (single temp., corrected for B)	[2]
−10.99 ± 0.05	magnetic anisotropy	[22]
−11.34	dielectric & pressure virial coefficients	[20]
−11.93 ± 0.18	CCSD(T) computation	[19]

†value in [21] corrected using our B = (-0.50 ± 0.11) × 10^{-60} C^3 m^4 J^{-2}
‡value in [2] corrected using our B = (-0.50 ± 0.11) × 10^{-60} C^3 m^4 J^{-2} and $\Delta\alpha$ = (3.267 ± 0.098) × 10^{-40} C^2 m^2 J^{-1}

4.3 Carbon monoxide (CO)

4.3.1 Introduction

The electric quadrupole moment of carbon monoxide has been measured through the technique of EFGIB by three previous researchers, all working at room temperature [2, 4, 6]. In order to obtain a definitive quadrupole moment for this important species, we have undertaken a full temperature-dependent study, working with an ultra-high-purity (UHP) carbon monoxide sample with a stated 99.99% minimum purity, supplied by Afrox.

We have made use of the polarisability anisotropy $\Delta\alpha = (0.592 \pm 0.018) \times 10^{-40}$ $\mathrm{C^2\,m^2\,J^{-1}}$ as measured by Bogaard *et al.* [14]. Since no dielectric virial-coefficient data for carbon monoxide could be found in the literature, the dielectric constant of the gas was calculated from the following expression for the dielectric constant [23]

$$A + \frac{B}{T} = \frac{\epsilon_r - 1}{\epsilon_r + 2} V_m, \tag{4.4}$$

where V_m is the molar volume. The coefficients A and B may be determined from the equations [23]

$$A = \frac{N_A\, a_0}{3\,\epsilon_0} \tag{4.5}$$

and

$$B = \frac{N_A\, \mu_0^2}{9\,\epsilon_0\, k}, \tag{4.6}$$

where a_0 is the static mean polarisabilty and μ_0 is the dipole moment of the molecule.

Making use of the dipole moment of 0.3492×10^{-30} C m [23] and the a_o value of 2.17×10^{-40} $C^2\,m^2\,J^{-1}$ provided by Alms *et al.* [24], we were able to calculate ϵ_r from equation 4.4 as required.

4.3.2 Results

A number of experimental runs were performed at each temperature, and the results obtained for carbon monoxide are given in Table 4.8 below.

Table 4.8: The Buckingham constant ($_mQ$) values for carbon monoxide measured over a range of temperature and at 632.8 nm

$\overline{T}$ (K)	$P^\dagger$ (MPa)	$10^4 V_m{}^\dagger$ ($m^3\,mol^{-1}$)	$\varepsilon_r{}^\dagger$	$V^\dagger$ (kV)	$10^{-8} E_{xx}{}^\dagger$ ($V\,m^{-2}$)	$10^{26}\,{}_mQ^\ddagger$ ($C\,m^5\,J^{-1}\,mol^{-1}$)
301.2	2.305	10.81	1.014	3.064	-7.575	-4.069 ± 0.048
326.8	1.690	16.05	1.010	3.026	-8.069	-3.774 ± 0.056
354.6	1.475	20.07	1.008	3.048	-8.664	-3.482 ± 0.068
386.1	1.530	21.09	1.007	3.049	-8.667	-3.229 ± 0.063
423.7	1.345	26.34	1.006	3.059	-9.288	-2.959 ± 0.087
473.9	1.115	35.48	1.004	3.023	-9.655	-2.683 ± 0.077

† These values are for a typical run.

‡ This value is the average of all the runs (typically around 1000 null currents) obtained at a particular temperature.

4.3.3 Discussion

A plot of the above Buckingham-constant values versus inverse temperature is shown in Figure 4.3 below, together with the weighted best-fit straight line. The slope and intercept of the weighted fit are summarised in Table 4.9, together with the extracted quadrupole moment and hyperpolarisability.

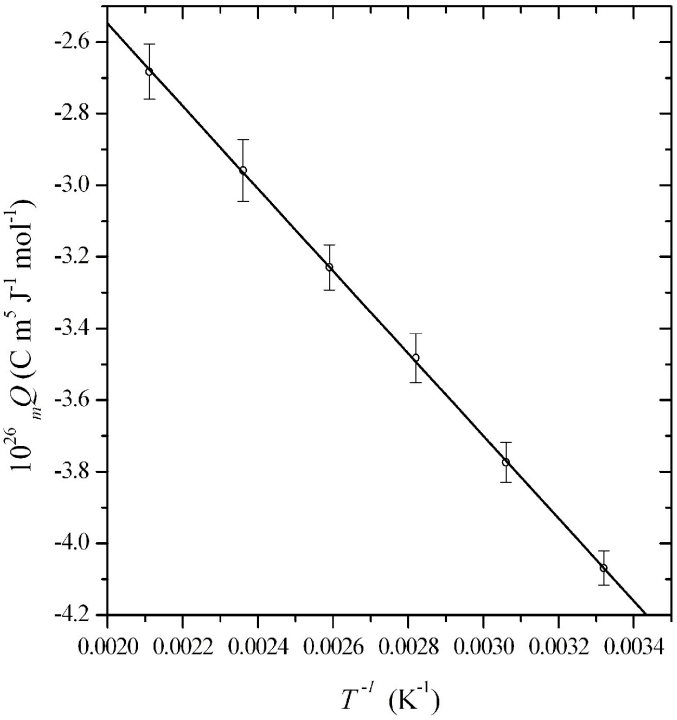

Figure 4.3: The temperature dependence of ${}_mQ$ for carbon monoxide

We obtain a quadrupole moment for carbon monoxide of Θ = (-8.87 $\pm$

Table 4.9: Slope and intercept values extracted from the ${}_mQ$ vs T^{-1} graph, literature polarizability anisotropy required for the analysis, together with the quadrupole moment and quadrupole hyperpolarisability of carbon monoxide determined via equation (2.5)

Property	Value
10^{26} intercept ($\mathrm{C\,m^5\,J^{-1}\,mol^{-1}}$)	-0.249 ± 0.016
10^{23} slope ($\mathrm{C\,m^5\,K\,J^{-1}\,mol^{-1}}$)	-1.1504 ± 0.0057
10^{40} $\Delta\alpha$ ($\mathrm{C^2\,m^2\,J^{-1}}$) [13]	0.592 ± 0.018
10^{40} Θ ($\mathrm{C\,m^2}$)	-8.87 ± 0.31
10^{60} B ($\mathrm{C^3\,m^4\,J^{-2}}$)	-0.1032 ± 0.0066

$0.31) \times 10^{-40}$ $\mathrm{C\,m^2}$, and a quadrupole hyperpolarisability of B = (-0.1032 $\pm$ 0.0066) $\times 10^{-60}$ $\mathrm{C^3\,m^4\,J^{-2}}$. To compare our quadrupole moment with the single-temperature measurement of Graham *et al.* [6], we need to re-analyse their data taking into account our quadrupole hyperpolarisability term. Assuming B to be negligible, they obtained Θ = (-9.47 $\pm$ 0.15) $\times 10^{-40}$ $\mathrm{C\,m^2}$. Including the effects of B, their revised value becomes Θ = (-8.88 $\pm$ 0.21) $\times 10^{-40}$ $\mathrm{C\,m^2}$, which agrees with our value to within 0.1%. The contribution of B to ${}_mQ$ at 301.2 K is some (6.2 $\pm$ 0.5)%, which is far from negligible, indicating the necessity of a temperature-dependent EFGIB study for this molecule if a definitive quadrupole moment is to be obtained.

Recent *ab initio* quantum computations of the quadrupole moment of carbon

Table 4.10: A comparison of selected molecular quadrupole moments for CO

$10^{40}\Theta$ (C m^2)	Method	Reference
-8.87 ± 0.31	EFGIB (temp. dependent)	this work
-9.47 ± 0.15	EFGIB (single temp., $B = 0$)	[6]
$-8.88 \pm 0.21^{\dagger}$	EFGIB (single temp., corrected for B)	[6]
$-8.58 \pm 0.35^{\ddagger}$	EFGIB (single temp., $B = 0$)	[4]
-8.3 ± 1.0	EFGIB (single temp., $B = 0$)	[2]
-9.14 ± 0.22	CCSD(T) computation	[19]

†value in [6] corrected using our $B = (\text{-}0.1032 \pm 0.0066) \times 10^{-60}$ C^3 m^4 J^{-2}
‡here, as discussed in Chapter 2, the quarter-wave plate was offset, leading to quadrupole moments up to 8% in error

monoxide have been obtained at the CCSD(T) level of theory [19], yielding a value of $\Theta = (\text{-}9.14 \pm 0.22) \times 10^{-40}$ C m^2. This value is relative to the effective quadrupole centre (rather than to the centre-of-mass), and so may be compared directly with our measured value for this polar molecule. Theory and experiment are seen to agree to within 3.0%, and it seems safe to conclude that the quadrupole moment for carbon monoxide is now definitively known. The computed quadrupole hyperpolarisability of $B = \text{-}0.118 \times 10^{-60}$ C^3 m^4 J^{-2} lies within two standard deviations of our measured value.

4.4 Hydrogen (H_2)

4.4.1 Introduction

Only one previous EFGIB measurement of the quadrupole moment of hydrogen has been attempted [2]. The recent *ab initio* quantum-computational investigation of EFGIB in hydrogen [25] using Coupled Cluster Singles and Doubles (CCSD) response theory has prompted us to undertake a definitive experimental investigation of EFGIB for this molecule. Work was performed using a cylinder of UHP hydrogen, supplied by Air Products, and with a stated minimum purity of 99.999%. Extreme caution was exercised when handling this gas. The cell was initially filled with helium, and a Spectron model 300E helium leak detector was used to establish the sources of even very tiny leaks, which were then sealed up. Once measurements on hydrogen were completed, used samples were burnt off in a controlled manner.

The second and third pressure virial coefficients used to calculate the molar volume were obtained from the most recent Dymond *et al.* tabulations [12]. Values for the dielectric virial coefficients were obtained from Watson *et al.* [26], while the polarisability anisotropy has been accounted for by using the value of $\Delta\alpha = (0.349 \pm 0.011) \times 10^{-40}\ \mathrm{C^2\,m^2\,J^{-1}}$ obtained by Bridge and Buckingham [27].

The effects of quantization on the rotational motion of hydrogen are too

pronounced to be ignored, and so the equation for the molar Buckingham constant in (1.46) obtained using classical theory needs to be corrected for quantum effects. This has been reviewed in Section 1.3.2, where for non-polar molecules we obtain

$$ {}_mQ = \frac{2\left(3\epsilon_r + 2\right) N_A}{225\epsilon_r\epsilon_0}\left[\frac{15}{2}B + \frac{\Delta\alpha\,\Theta}{kT}\right]., \tag{4.7} $$

where

$$ f(T) = 1 - \left[\frac{\hbar^2}{2kTI}\right] + \frac{8}{15}\left[\frac{\hbar^2}{2kTI}\right]^2 - \cdots \tag{4.8} $$

for a linear molecule with I being its principal moment of inertia. Using the moments of inertia provided by Moore [28] we obtain the following values for $f(T)$:

Table 4.11: Values for $f(T)$ at various temperatures for hydrogen

T (K)	$f(T)$
300	0.753
333	0.773
358	0.787
393	0.803
440	0.820
474	0.833

4.4.2 Results

The experimental results for hydrogen are shown in Table 4.12. Owing to the tiny signal for this molecule, with typical retardances being of the order of 30 nrad, a large number of runs was required.

Table 4.12: The Buckingham constant ($_mQ$) values for hydrogen measured over a range of temperature and at 632.8 nm

$\overline{T}$ (K)	$P^\dagger$ (MPa)	$10^4 V_m{}^\dagger$ ($m^3\,mol^{-1}$)	$\varepsilon_r{}^\dagger$	$V^\dagger$ (kV)	$10^{-8} E_{xx}{}^\dagger$ ($V\,m^{-2}$)	$10^{26}\,{}_mQ^\ddagger$ ($C\,m^5\,J^{-1}\,mol^{-1}$)
301.2	0.715	3.496	1.0020	3.047	-7.640	0.488 ± 0.018
333.1	0.555	4.998	1.0010	3.675	-8.309	0.460 ± 0.019
358.4	0.455	5.386	1.0010	3.034	-8.219	0.442 ± 0.017
393.7	0.455	7.289	1.0010	3.059	-8.135	0.415 ± 0.020
436.7	0.475	7.777	1.0008	3.049	-7.626	0.387 ± 0.022
474.8	0.545	7.266	1.0009	3.029	-7.953	0.368 ± 0.026

† These values are for a typical run.

‡ This value is the average of all the runs (typically around 2000 null currents) obtained at a particular temperature.

4.4.3 Discussion

A plot of the above Buckingham-constant values versus $\frac{f(T)}{T}$ is shown in Figure 4.4 below, together with the weighted best-fit straight line. The slope and intercept of the weighted fit are summarised in Table 4.13, together with the extracted quadrupole moment and hyperpolarisability.

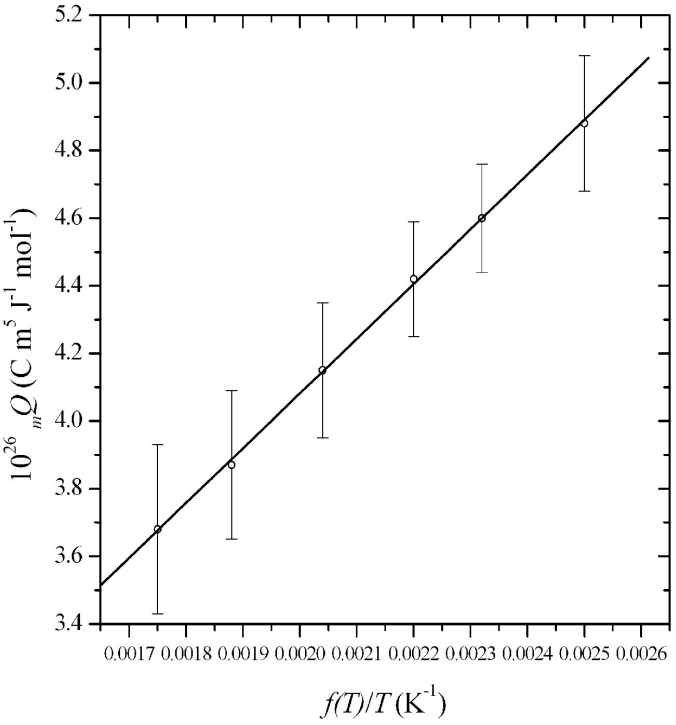

Figure 4.4: The temperature dependence of ${}_mQ$ for hydrogen

Our value of $\Theta = (2.12 \pm 0.11) \times 10^{-40}\ \mathrm{C\,m^2}$ for the electric quadrupole mo-

Table 4.13: Slope and intercept values extracted from the ${}_mQ$ vs $\frac{f(T)}{T}$ graph, literature polarizability anisotropy required for the analysis, together with the quadrupole moment and quadrupole hyperpolarisability of hydrogen determined via equation (2.5)

Property	Value
10^{28} intercept ($\mathrm{C\,m^5\,J^{-1}\,mol^{-1}}$)	0.84 ± 0.33
10^{24} slope ($\mathrm{C\,m^5\,K\,J^{-1}\,mol^{-1}}$)	1.618 ± 0.034
10^{40} $\Delta\alpha$ ($\mathrm{C^2\,m^2\,J^{-1}}$) [27]	0.349 ± 0.011
10^{40} Θ ($\mathrm{C\,m^2}$)	2.12 ± 0.11
10^{60} B ($\mathrm{C^3\,m^4\,J^{-2}}$)	0.0037 ± 0.0014

ment of hydrogen agrees to within 2.1% with the recent *ab initio* computed value of 2.166 $\times 10^{-40}$ $\mathrm{C\,m^2}$ obtained by Buckingham *et al.* using CCSD response theory [25]. This computed value agrees well with the much earlier computation of Kolos and Wolniewicz [26-28], which yielded 2.17 $\times 10^{-40}$ $\mathrm{C\,m^2}$.

The only previous EFGIB measurement of hydrogen is that of Buckingham *et al.* [2], which was performed at a room temperature of 297.15 K. Here the quantity $(n_x - n_y)V_m/N_A E_{xx}$ was measured to be $(0.018 \pm 0.003) \times 10^{-36}$ esu, which yields a molar Buckingham constant of ${}_mQ = (2.41 \pm 0.41) \times 10^{-27}$ $\mathrm{C\,m^5\,J^{-1}\,mol^{-1}}$ for $T = 297.15$ K. Our measured ${}_mQ$ at $T = 301.2$ K is $(4.88 \pm 0.18) \times 10^{-27}$ $\mathrm{C\,m^5\,J^{-1}\,mol^{-1}}$, some 2.02 times larger than the

Buckingham *et al.* result. Buckingham *et al.* used the computed quadrupole moment [30-32] to extract a hyperpolarisability of $B = (-7.8 \pm 2.6) \times 10^{-62}$ $C^3\,m^4\,J^{-2}$. Their recent computed value is -6.87×10^{-62} $C^3\,m^4\,J^{-2}$; while our experimental value is some 18 times smaller in magnitude, at $(0.37 \pm 0.14) \times 10^{-62}$ $C^3\,m^4\,J^{-2}$. Whereas the Buckingham 'experimental' B yields a contribution to ${}_mQ$ of $(-72 \pm 24)\%$, ours yields a much smaller, but definitely non-negligible, contribution of $(10.0 \pm 4.0)\%$.

While we can conclude that the quadrupole moment of hydrogen has now been definitively determined by EFGIB experiment, there still exists a substantial discrepancy between the experimental and theoretical quadrupole hyperpolarisability values. It is anticipated that future computational work, perhaps together with an independent temperature-dependent EFGIB experimental study, will resolve this discrepancy.

Table 4.14: A comparison of selected molecular quadrupole moments for H_2

$10^{40}\Theta$ ($C\,m^2$)	Method	Reference
2.12 ± 0.11	EFGIB (temp. dependent)	this work
2.17	*ab initio* computation	[29]
2.166	CCSD computation	[25]

Table 4.15: A comparison of quadrupole hyperpolarisabilities for H_2

$10^{62}B$ ($C^3\,m^4\,J^{-2}$)	Method	Reference
0.37 ± 0.12	EFGIB (temp. dependent)	this work
$-7.8 \pm 2.6^{\dagger}$	EFGIB (single temp.)	[2]
-6.87	CCSD computation	[25]

†extracted from the measured data assuming $\Theta = 2.17 \times 10^{-40}$ C m^2 [30-32]

4.5 Carbonyl Sulphide (OCS)

Only one previous experimental determination of the quadrupole moment of carbonyl sulphide by the EFGIB technique exists [2], and the investigation was performed at room temperature. A recent *ab initio* quantum-computational study [17] of this molecule at the CCSD level of theory prompted us to attempt a temperature-dependent study. However, for reasons to be explained shortly, we were only able to achieve measurements at room temperature. Work was performed on a high-purity sample of carbonyl sulphide with a quoted minimum purity of 99.95%, supplied by Intergas.

The polarisability anisotropy used in our calculations is the value of $(4.53 \pm 0.13) \times 10^{-40}$ $\mathrm{C^2\,m^2\,J^{-1}}$ measured at 632.8 nm by Bogaard *et al.* [14]. The virial coefficient data provided by Ihmels and Gmehling [33] were used in the calculation of the pressure virial coefficients. No dielectric virial coefficient data for carbonyl sulphide could be found, and so the alternative method as outlined for carbon monoxide was used to calculate the dielectric constant of the gas. A value of 2.365×10^{-30} C m for the dipole moment μ [29, 30], and a value of 6.353×10^{-40} $\mathrm{C^2\,m^2\,J^{-1}}$ for the static polarisability a_0 [23], were used in these calculations.

4.5.1 Results

A number of runs were performed on carbonyl sulphide at a room temperature ranging from 22 to 29 °C over the course of the measurements. The measured data are summarised in Table 4.16.

Table 4.16: The Buckingham constant ($_mQ$) value for carbonyl sulphide measured at room temperature and at 632.8 nm

$\overline{T}$ (K)	$P^\dagger$ (MPa)	$10^4 {V_m}^\dagger$ ($m^3\,mol^{-1}$)	${\varepsilon_r}^\dagger$	$V^\dagger$ (kV)	$10^{-8} {E_{xx}}^\dagger$ ($V\,m^{-2}$)	$10^{26}\,{}_mQ^\ddagger$ ($C\,m^5\,J^{-1}\,mol^{-1}$)
302.1	0.725	3.239	1.023	3.036	-8.491	-0.323 ± 0.019

† These values are for a typical run.

‡ This value is the average of all the runs (around 3000 null currents).

From our single-temperature measurement the molecular quadrupole moment of OCS is calculated to be (-0.984 ± 0.048) × 10^{-40} C m^2, assuming the quadrupole hyperpolarisability contribution to be zero. Although this value is in excellent accord with the experimental value of (-0.99 ± 0.32) × 10^{-40} C m^2 obtained by Buckingham *et al.* [2], it is not in agreement with the CCSD computed value of (-0.031 ± 0.224) ×10^{-40} C m^2 obtained by Coriani *et al.* [19]. This computed value, which is relative to the effective quadrupole centre, has very large uncertainty bounds, and its comparison with the experimental values is not at all satisfactory, suggesting the need for further investigation. If we re-analyse our experimental quadrupole moment taking into account the computed hyperpolarisability of B = -0.41 × 10^{-60} [19], we obtain Θ = (-0.842 ± 0.053). This reduces the magnitude of the quadrupole moment by some 14%.

It is clear that a definitive experimental estimate of the quadrupole moment of this molecule requires a full temperature-dependent study of the EFGIB. Unfortunately, our persistent attempts to perform measurements at higher temperatures proved fruitless. At temperatures even 30°C above room temperature, a deposit was found to form on the cell entrance and exit windows. This deposit was a combination of a blackish sooty substance as well as a yellow deposit that strongly resembled flowers of sulphur, suggesting decomposition of OCS into solid carbon and sulphur, as well as unknown gases. This deposit quickly accumulated, preventing the laser beam from passing

through the cell, and hence rendering measurements above room temperature impossible. Several enquiries with researchers active in the field of thermal decomposition of molecules, to determine the cause of this formation, have to date proved futile. Further attempts at measurements on this molecule will continue, and hopefully results will be forthcoming. Until then, knowledge of the quadrupole moment of carbonyl sulphide remains ambiguous, the extent of the hyperpolarisability contribution remaining unknown.

4.6 Concluding remarks

Recent *ab initio* quantum-computational studies of the molecular electric quadrupole moments and quadrupole hyperpolarisabilities of the carbon dioxide, nitrous oxide, carbon monoxide and hydrogen molecules [17, 18, 19, 25] have prompted us to undertake an experimental EFGIB temperature-dependent investigation of these molecules. This has allowed us to ascertain the extent of the hyperpolarisability term contributions to their molar Buckingham constants, and to extract definitive quadrupole moments. This has made possible a definitive comparison of experiment and theory for these important species.

Although the quadrupole moment of carbonyl sulphide has also recently been calculated [19], thermal decomposition of this molecule at tempera-

tures higher than the room temperature has meant that our EFGIB study has been limited to a single temperature, so that the quadrupole moment reported here is not definitive, the hyperpolarisability contribution having been assumed to be negligible.

Bibliography

[1] A. D. Buckingham and R. L. Disch, *Proc. R. Soc. ,* **A 273**, 273 (1963)

[2] A. D. Buckingham, R. L. Disch, and D. A. Dunmur, *J, Am. chem. Soc.,* **90**, 3104 (1968)

[3] M. R. Battaglia, A. D. Buckingham, D. Neumark, R. K. Pierens, and J. H. Williams, *Molec. Phys.,* **43**, 1015 (1981)

[4] C. Graham, J. Pierrus, and R. E. Raab, *Molec. Phys.,* **67**, 939 (1989)

[5] J. N. Watson, I. E. Craven, and G. L. D. Ritchie, *Chem. Phys. Lett,* **274**, 2 (1997)

[6] C. Graham, D. A. Imrie, and R. E. Raab, *Molec. Phys.,* **93**, 49 (1998)

[7] T. H. Spurling and E. A. Mason, *J. Chem. Phys.,* **46**, 322 (1967)

[8] T. K. Bose and R. H. Cole, *J. Chem. Phys.,* **52**, 140 (1970)

[9] M. Bloom, I. Oppenheim, M. Lipsicas, C. G. Wade, and C. F. Yarnell, *J. Chem. Phys.,* **43**, 1036 (1965)

[10] W. Ho, G. Birnbaum, and A. Rosenberg, *J. Chem. Phys.,* **55**, 1028 (1971)

[11] D. R. Johnston and R. H. Cole, *J. Chem. Phys.,* **36**, 318 (1971)

[12] J. H. Dymond, K. N. Marsh, R. C. Wilhoit, and K. C. Wong, *The virial coefficients of pure gases and mixtures,* **Springer**, (2002)

[13] A. D. Buckingham, *J. Chem. Phys. ,* **30**, 1580 (1959)

[14] M. P. Bogaard, A. D. Buckingham, R. K. Pierens, and A. H. White, *Trans. Faraday Soc.,* **74**, 3008 (1978)

[15] H. Kling and W. Hüttner, *J. Chem. Phys.,* **90**, 207 (1984)

[16] A. J. Russell and M. A. Spackman, personal communication to G. L. D. Ritchie [5]

[17] S. Coriani, A. Halkier, A. Rizzo, and K. Ruud, *Chem. Phys. Lett.,* **326**, 269 (2000)

[18] G. Maroulis, *Chem. Phys.,* **291**, 81 (2003)

[19] S. Coriani, A. Halkier, D. Jonsson, J. Gauss. A. Rizzo, and O. Christiansen, *J. Chem. Phys.,* **118**, 7329 (2003)

[20] S. Kirouac and T. K. Bose, *J, Chem. Phys.,* **59**, 3043 (1973)

[21] A. D. Buckingham, C. Graham, and J. H. Williams, *Molec. Phys.,* **49**, 703 (1983)

[22] J. M. L. J. Reinartz, W. L. Meerts, and A. Dymanus, *Chem. Phys.,* **31**, 19, (1978)

[23] A. A. Maryott and F. Buckley, *Circ. US Natn. Bur. Stand.* **537**, 11 (1953)

[24] G. R. Alms, A. K. Burnham, and W. H. Flygare, *J. Chem. Phys.,* **63**, 3321 (1975)

[25] A. D. Buckingham, S. Coriani, and A. Rizzo, *Theor. Chem. Acc.,* **117**, 969 (2007)

[26] H. E. Watson, G. Gundu Roa, and K. L. Ramaswamy, *Proc. Roy. Soc.,* **132**, 569 (1932)

[27] N. J. Bridge and A. D. Buckingham, *Proc. Roy. Soc. Lond. A,* **295**, 334 (1966)

[28] W. J. Moore, *Physical Chemistry,* 5th edition (Longman) (1972)

[29] D. E. Stogryn and A. P. Stogryn, *Mol. Phys.,* **11**, 371 (1966)

[30] A. L. McClellan, *Tables of Experimental Dipole Moments,* (W. H. Freeman and Co.) (1963)

[31] W. Kolos and L. Wolniewicz, *J. Chem. Phys.,* **41**, 3674 (1964)

[32] L. Wolniewicz, *J. Chem. Phys.,* **45**, 515 (1966)

[33] E. Ihmels and J. Gmehling, *Ind. Eng. Chem. Res.,* **40**, 4470 (2001)